[American Journal of Science, Vol. 307, June, 2007, P. 861–900, DOI 10.2475/06.2007.01]

American Journal of Science

JUNE 2007

GENERALIZATION OF GAS HYDRATE DISTRIBUTION AND SATURATION IN MARINE SEDIMENTS BY SCALING OF THERMODYNAMIC AND TRANSPORT PROCESSES

GAURAV BHATNAGAR*, WALTER G. CHAPMAN*, GERALD R. DICKENS**, BRANDON DUGAN**, and GEORGE J. HIRASAKI*†

ABSTRACT. Gas hydrates dominated by methane naturally occur in deep marine sediment along continental margins. These compounds form in pore space between the seafloor and a sub-bottom depth where appropriate stability conditions prevail. However, the amount and distribution of gas hydrate within this zone, and free gas below, can vary significantly at different locations. To understand this variability, we develop a one-dimensional numerical model that simulates the accumulation of gas hydrates in marine sediments due to upward and downward fluxes of methane over time. The model contains rigorous thermodynamic and component mass balance equations that are solved using expressions for fluid flow in compacting sediments. The effect of salinity on gas hydrate distribution is also included.

The simulations delineate basic modes of gas hydrate distribution in marine sediment, including systems with no gas hydrate, gas hydrate without underlying free gas, and gas hydrate with underlying free gas below the gas hydrate stability zone, for various methane sources. The results are scaled using combinations of dimensionless variables, particularly the Peclet number and Damkohler number, such that the dependence of average hydrate saturation on numerous parameters can be summarized using two contour maps, one for a biogenic source and one for upward flux from a deeper source. Simulations also predict that for systems at steady state, large differences in parameters like seafloor depth, seafloor temperature and geothermal gradient cause only small differences in average hydrate saturation when examined with scaled variables, although important caveats exist. Our model presents a unified picture of hydrate accumulations that can be used to understand well-characterized gas hydrate systems or to predict steady-state average hydrate saturation and distribution at locations for which seismic or core data are not available.

INTRODUCTION

Natural gas hydrates can precipitate in pore space of deep-sea sediments when gas concentrations exceed saturation at appropriate stability conditions (Kvenvolden, 1993; Dickens, 2001). In general, these conditions occur between the seafloor and a relatively shallow, sub-bottom depth where temperatures become excessively warm because of the geotherm (fig. 1). The depth interval is commonly called the gas hydrate stability zone (GHSZ), and its lower boundary is often underlain by free gas (Kvenvolden, 1993; Dickens, 2001).

Enormous amounts of methane reside as gas hydrate and associated free gas along continental margins. Although global estimates vary widely (Dickens, 2001; Buffett and Archer, 2004; Milkov, 2004; Klauda and Sandler, 2005), oceanic gas hydrates and free gas may constitute a possible energy resource (Collett, 2002) and large component of

*Rice University, Department of Chemical and Biomolecular Engineering, Houston, Texas 77005; gb@rice.edu

**Rice University, Department of Earth Science, Houston, Texas 77005

†Corresponding author: gjh@rice.edu

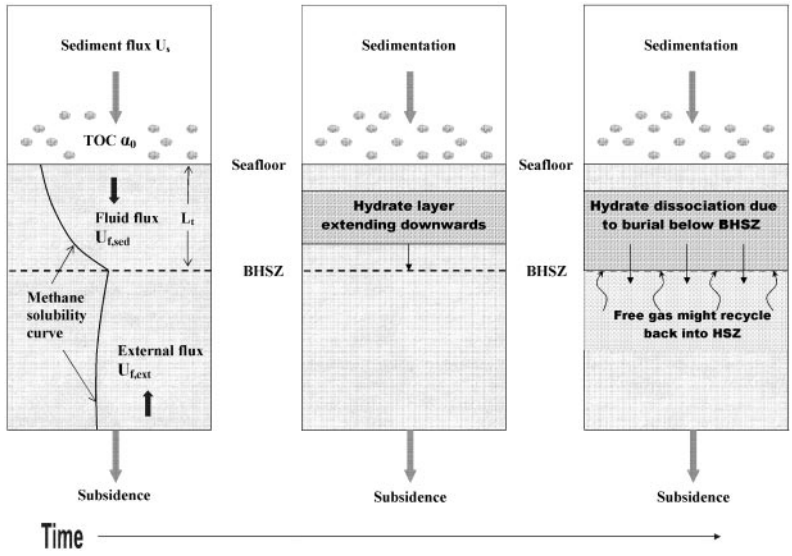

Fig. 1. Schematic of our model showing gas hydrate evolution in time. Left: Methane fluxes from top (methanogenic source) and below (deeper source) along with model parameters and methane solubility curve. L, H and V represent conditions for stability of liquid, hydrate and free gas phases, respectively; Middle: Gas hydrate layer developing and moving towards the base of the gas hydrate stability zone (GHSZ) due to sedimentation; Right: Steady state might result in free gas below gas hydrate and methane recycling at the base of the GHSZ.

the global carbon cycle (Kvenvolden, 1988; Dickens, 2003). As their stability depends on pressure and temperature, gas hydrates may also represent a geohazard during oil recovery (Briaud and Chaouch, 1997; Borowski and Paull, 1997), a cause of slope failure (Maslin and others, 2004; Sultan and others, 2004), and source of methane during past intervals of rapid oceanographic change (Dickens and others, 1995; Hesselbo and others, 2000). A good appreciation of these issues requires an understanding of how gas hydrates accumulate in marine sediment sequences over time.

Results of the Ocean Drilling Program (ODP), particularly Legs 164 and 204, have greatly enhanced our understanding of gas hydrate distribution along active and passive margins (Paull and others, 1996; Trehu and others, 2003). Unquestionably, at many locations, lithology dictates gas hydrate distribution at the local scale (Kraemer and others, 2000; Weinberger and others, 2005). More important, however, are regional scale variations in gas hydrate distribution between and within different geologic settings. For example, outer Blake Ridge (Leg 164) offshore South Carolina has modest quantities of gas hydrate dispersed over immense volumes of sediment, but locations with and without free gas beneath the GHSZ (Paull and Matsumoto, 2000). By contrast, Hydrate Ridge (Leg 204) on the Cascadia Margin offshore Oregon has widely varying gas hydrate contents distributed across small volumes of sediment usually underlain by free gas (Tréhu and others, 2004).

Marine gas hydrates are components of complex systems with dynamic inputs and outputs of methane over time (Dickens, 2003). Excepting at select sites (for example, some seeps in the Gulf of Mexico), most gas within marine gas hydrates is methane (Kvenvolden, 1993; Milkov, 2005). However, this methane may derive from two general reactions, and gas hydrates may form through two general processes. At relatively low temperatures, characteristic of sediments at shallow burial depths, methanogenic archaea form biogenic methane; at relatively high temperatures, such

as found deep within sediment sequences, thermo-catalytic reactions produce thermogenic methane (Claypool and Kvenvolden, 1983; Whiticar and others, 1986). Gas hydrates have been recovered from marine sediment with constituent methane principally derived from biogenic or thermogenic reactions (Kvenvolden, 1993; Milkov, 2005). More crucially, biogenic methane can be supplied within the GHSZ during burial of organic carbon (*in situ* methane) or to the GHSZ through upward migration of methane bearing fluids (deep methane). The first input appears to dominate some gas hydrate systems, such as on outer Blake Ridge (Paull and others, 1994; Egeberg and Dickens, 1999), while the second appears to dominate other systems, such as along Cascadia Margin (Hyndman and Davis, 1992; Haeckel and others, 2004; Torres and others, 2004). Outputs of methane from gas hydrate systems include advection and diffusion (Xu and Ruppel, 1999). Given the known variations in natural gas hydrate systems, an important issue is whether relatively simple and straightforward numerical models can explain general features of all systems. In particular, can changes in a few basic factors encompass a wide range of observations?

Previous numerical models for the accumulation of gas hydrate in marine sediment have focused mainly on simulating the distribution of gas hydrate at specific sites using parameters relevant to those locations. Blake Ridge (Egeberg and Dickens, 1999; Davie and Buffett, 2001, 2003a; Gering, 2003) and Hydrate Ridge (Luff and Wallmann, 2003; Haeckel and others, 2004; Torres and others, 2004; Liu and Flemings, 2006) have been the subject of most studies. These models yield hydrate profiles fairly consistent with proxy evidence, but give little insight as to how changes in basic parameters alter the dynamics and distribution of gas hydrate. Studying effects of parameter changes in these models through sensitivity analysis requires new simulations to be performed for the perturbed parameter around its base case value. Thus, separate hydrate provinces are studied as isolated examples without common processes connecting them together. We acknowledge that heterogeneous gas hydrate distribution at the local scale necessitates modeling that accounts for detailed geology and structure, probably in two or three spatial dimensions. However, a first-order modeling in one-dimension has the advantage of providing a simple understanding for how various processes affect natural gas hydrate systems.

In this paper, we develop a numerical model for gas hydrate accumulation in marine sediments over geologic time scales. Using this model, we show that gas hydrate distributions in various locations can be described in terms of a few dimensionless groups or variables. This allows different gas hydrate systems to be classified and linked from a mechanistic perspective.

NOTATION

c_i^j, $\tilde{c}_i^j$	mass fraction and normalized value of component i in phase j, respectively
$c_{m,eqb}^l$	methane mass fraction in the pore fluid at GHSZ depth
C_i	Langmuir constant for cavity type i
D_m, Da	methane diffusivity and Damkohler number, respectively
f_{CH_4}	methane fugacity
L_t, L_Φ	depth to base of GHSZ and characteristic compaction length, respectively
$N_{t\Phi}$	ratio of GHSZ depth to characteristic compaction length
p, P	pressure
Pe_1, Pe_2	Peclet numbers for compaction driven and external flow, respectively
S_i	saturation of phase i
t, $\tilde{t}$	dimensional time and dimensionless time, respectively
T	temperature

U_f, U_s	net fluid flux and sediment flux, respectively
$U_{f,sed}$, U_{ext}	fluid flux due to sedimentation and upward external flow, respectively
$\tilde{U}_f$, $\tilde{U}_s$	dimensionless net fluid flux and sediment flux, respectively
v_i	ratio of number of type i cavities to number of water molecules
v_s	sediment velocity
x_i	mole fraction of component i in aqueous phase
z, $\tilde{z}$	vertical depth and normalized vertical depth, respectively
α, $\tilde{\alpha}$	organic concentration in sediment and normalized value, respectively
α_0, β	organic content at seafloor and normalized value, respectively
Δh_w, Δv_w, $\Delta\mu_w^{l,0}$	enthalpy, volume and chemical potential difference between empty hydrate lattice and water, respectively
ϕ, $\tilde{\phi}$	sediment porosity and reduced sediment porosity, respectively
ϕ_0, ϕ_∞	sediment porosity at seafloor and minimum porosity at depth, respectively
γ, η	reduced porosity parameters
γ_w	activity coefficient of water
λ	rate of methanogenesis
μ_i^j	chemical potential of component i in phase j
θ_i	fractional occupancy of cage type i
ρ_i, $\tilde{\rho}_i$	density of phase i and ratio of phase i to water density, respectively
σ_e, σ_v, σ_ϕ	effective, total and characteristic stress for compaction, respectively

Subscripts

m, w	methane and water components, respectively
g, h, f, s	free gas, hydrate, water and sediment phases, respectively

Superscripts

g, h, w, β	free gas, hydrate, water and hypothetical empty lattice phases, respectively

QUANTITATIVE STUDIES OF NATURAL GAS HYDRATES

The base and thickness of the GHSZ (fig. 1) depend on pressure (water depth), temperature at the seafloor, the geotherm, pore water salinity, and gas composition (Dickens, 2001). In most places, gas hydrate only exists within a portion of the GHSZ because certain depth intervals, especially near the seafloor, do not contain sufficient methane (Dickens and others, 1997; Milkov and others, 2003). A Bottom Simulating Reflector (BSR) imaged on reflection seismic data often, but not always, marks the phase boundary between the base of the GHSZ and the underlying free gas stability zone (Kvenvolden, 1993; Paull and Matsumoto, 2000; Tréhu and others, 2004).

The amount and distribution of gas hydrate within the GHSZ at a given location can be quantified by several indirect techniques (Paull and Matsumoto, 2000; Tréhu and others, 2004). These include analyses of pressurized sediment cores, pore fluid geochemistry, sediment thermal anomalies, well-log velocity and resistivity, and seismic profiles. In concert, such methods can provide a current "snapshot" for the presence and abundance of gas hydrate (Paull and Matsumoto, 2000; Tréhu and others, 2004). However, they give no physical insight as to how the gas hydrate formed or the processes governing the accumulation.

The amount and distribution of gas hydrate in marine sediment can also be examined using numerical models, essentially considering the observables as the consequence of methane inputs and outputs over time (Rempel and Buffett, 1997;

Egeberg and Dickens, 1999; Davie and Buffett, 2001, 2003a; Gering, 2003; Luff and Wallmann, 2003; Haeckel and others, 2004; Torres and others, 2004; Liu and Flemings, 2006). To various degrees, most of these models use thermodynamic principles coupled with heat and mass transport equations in porous media to understand gas hydrate distribution, especially at Blake Ridge or Hydrate Ridge. However, in general, they do not incorporate both *in-situ* and deep methane sources in a systematic manner. Moreover, most of these transport models employ a hydrate phase balance, which requires the use of a rate law to model the kinetics of hydrate formation (Davie and Buffett, 2001; Haeckel and others, 2004; Torres and others, 2004). Our model differs from existing models in using component balances so that the system is in thermodynamic equilibrium over geologic time scales, which avoids the use of a kinetic model for hydrate formation. Further, we systematically incorporate both local and deeper sources of methane. The main difference, however, lies in the way we nondimensionalize our system, which leads to the characterization of different hydrate distributions using a few dimensionless groups. This enables depiction of average hydrate saturations in different geological settings with just two contour plots, which are valid for a wide range of model parameters. We also include the effect of salinity on gas hydrate distributions so they are pertinent to marine environments.

OVERALL MODEL FRAMEWORK

Our numerical model (fig. 1) for simulating gas hydrate accumulation consists of three main parts: (1) definition of appropriate phase equilibrium and methane solubility curves, (2) incorporation of sediment deposition and porosity reduction, and (3) an account of mass balances for methane, water and organic content. Phase equilibrium curves delineate the GHSZ and free gas stability zone, while methane solubility curves determine the concentration of methane necessary to produce gas hydrate or free gas bubbles in each of these regions. Continuous sedimentation supplies the organic carbon required to form methane through biogenic reactions, while compaction drives water flux within the sediments. Finally, mass balances allow for the transport of methane in the various phases. Gas hydrate or free gas phases appear whenever the dissolved methane concentration exceeds the local solubility within or below the GHSZ, respectively.

PHASE EQUILIBRIUM AND METHANE SOLUBILITY

Definition

Gas hydrates can coexist with aqueous and vapor phases at specific conditions defined by a three-phase equilibrium curve (Sloan, 1998). At temperatures lower than and at pressures higher than the three-phase equilibrium curve, gas hydrate is stable. In sediment sequences, increasing temperature along a geotherm limits gas hydrate to some finite sub-bottom depth (fig. 1). Gas hydrates can coexist with the aqueous phase in this L-H zone. Below, free gas can coexist with the aqueous phase in the L-V zone.

The thickness of the GHSZ in the marine realm is primarily governed by seafloor depth, seafloor temperature, the geotherm, and pore water salinity (Dickens, 2001). Capillary inhibition due to fine-grained sediments and gas composition may also impact the GHSZ thickness (Clennell and others, 1999; Milkov and Sassen, 2000). However, the first effect is probably minor given the close correspondence of theoretical and actual GHSZ depths found during recent drilling expeditions (Tréhu and others, 2004), and the second effect is probably trivial except in special cases (for example, seep locations with thermogenic gas). Consequently, we focus on the phase diagram and modeling of structure I hydrates.

Three Phase Equilibrium Curve

The three-phase equilibrium curve of gas hydrates is predicted using the statistical thermodynamic approach of van der Waals and Platteeuw (1959). The condition for three phase stability comes from the equality of the chemical potential of water in the hydrate and aqueous phases:

$$\mu_w^h = \mu_w^l \Rightarrow \mu_w^\beta - \mu_w^h = \mu_w^\beta - \mu_w^l \tag{1}$$

where μ_w^h, μ_w^l and μ_w^β are the chemical potentials of water in the hydrate phase, the aqueous phase and a reference hypothetical empty gas hydrate lattice, respectively. The difference in chemical potential between the reference state and the liquid phase can be calculated using a simplified relationship first proposed by Holder and others (1980):

$$\frac{\mu_w^\beta - \mu_w^l}{RT} = \frac{\Delta\mu_w^{l,0}}{RT_0} - \int_{T_0}^{T} \frac{\Delta h_w}{RT^2}\, dT + \int_0^P \frac{\Delta v_w}{RT}\, dP - \ln(\gamma_w x_w) \tag{2}$$

where $\Delta\mu_w^{l,0}$ is an experimentally determined chemical potential difference between the empty reference state and pure water at reference temperature (T_0) and zero absolute pressure, Δh_w and Δv_w are the enthalpy difference and volume difference between empty hydrate lattice and pure water, respectively, γ_w is the activity coefficient of water, and x_w is the mole fraction of water in the aqueous phase. To find the solubility of methane in water, we use an established equation of state for methane (Duan and others, 1992).

The difference in chemical potential between the reference empty hydrate lattice and the filled structure can be written as (Parrish and Prausnitz, 1972):

$$\frac{\mu_w^\beta - \mu_w^h}{RT} = -\sum_{i=1}^{2} v_i \ln(1 - \theta_i) \tag{3}$$

where the summation is done over both cage types in structure I hydrate, v_i is the ratio of type i cavities to the number of water molecules in the hydrate structure, and θ_i is fractional occupancy of type i cavity by gas molecules. The dependence of cage occupancies on gas fugacity is given by the following Langmuir type relation (Parrish and Prausnitz, 1972):

$$\theta_i = \frac{C_i f_{CH_4}}{1 + C_i f_{CH_4}} \tag{4}$$

where f_{CH_4} is the fugacity of methane in the gas phase, calculated using an equation of state (Peng and Robinson, 1976), and C_i corresponds to the Langmuir constant of adsorption for the small and large cages of structure I hydrate. Parameters used to evaluate the Langmuir constants and other thermodynamic reference properties were taken from Cao and others (2002) and Sloan (1998). The equality of chemical potentials can then be recast into the following residual form as a function of pressure:

$$g(P) = \frac{\Delta\mu_w^{l,0}}{RT_0} - \int_{T_0}^{T} \frac{\Delta h_w}{RT^2}\, dT + \int_0^P \frac{\Delta v_w}{RT}\, dP - \ln(\gamma_w x_w) + \sum_{i=1}^{2} v_i \ln\left(1 - \frac{C_i f_{CH_4}}{1 + C_i f_{CH_4}}\right) = 0 \tag{5}$$

The parameters used in this formulation are listed in table 1. The root of this function $g(P)$ is the three phase equilibrium pressure, and it is evaluated using the Newton-Raphson method. The addition of dissolved ions changes the activity of water

Table 1

Thermodynamic reference properties[1]	Value	Reference
$\Delta\mu_w^{l,0}$	1236 J/mol	2
Δh_w^0	-4303.5 J/mol	2
$\Delta C_{p,w}^0$	-38.12 J/mol K	2
b	0.141 J/mol K^2	2
Δv_w	4.598 cm^3/mol	2
T_0	273.15 K	2
Transport parameters		
ρ_h	0.93 g/cm^3	3
ρ_s	2.65 g/cm^3	3
ρ_f	1.03 g/cm^3	
c_m^h	0.134	3
M_{CH_4}	16	3
M_{org}	30	3
Seafloor parameters		
$N_{t\phi}$	1	
ϕ_0	0.7	
ϕ_∞	0.1	

1) $\Delta h_w = \Delta h_w^0 + \int_{T_0}^{T} \Delta C_{P,w}\, dT$, where ; $\Delta C_{p,w} = \Delta C_{p,w}^0 + b(T - T_0)$
2) Cao and others (2002)
3) Davie and Buffett (2001)

($\gamma_w x_w$) in solution, which can be incorporated in equation (5) using Pitzer equations (Pitzer and Mayorga, 1973).

Equation (5) gives accurate pressures and temperatures for three phase equilibrium conditions (fig. 2). The equilibrium curve for the methane-pure water system agrees with experimental data (McLeod and Campbell, 1961; Marshall and others, 1964; Adisasmito and others, 1991; Yang and others, 2001) and predictions from the CSMHYD program (Sloan, 1998). Results for a 0.6m NaCl solution, which has water activity approximately equal to that of seawater (33.5‰ salinity), agree with experimental values (de Roo and others, 1983; Dickens and Quinby-Hunt, 1994).

The detailed modeling of the three-phase equilibrium allows us to calculate the cage occupancies of the small and large cages of structure I hydrate, which are later used to calculate the solubility of methane in equilibrium with the hydrate phase (L-H zone). This helps to build an accurate and thermodynamically rigorous methane solubility model compared to the approximate empirical relationships used in other transport models for hydrate accumulation (Xu and Ruppel, 1999; Davie and Buffett, 2001).

Methane Solubility in the GHSZ

Methane solubility within the GHSZ corresponds to the concentration of methane required to precipitate hydrate. It is known that methane solubility in equilibrium with gas hydrate in the L-H region rises with increasing temperature and drops with increasing pressure (Handa, 1990; Zatsepina and Buffett, 1998; Yang and others, 2001;

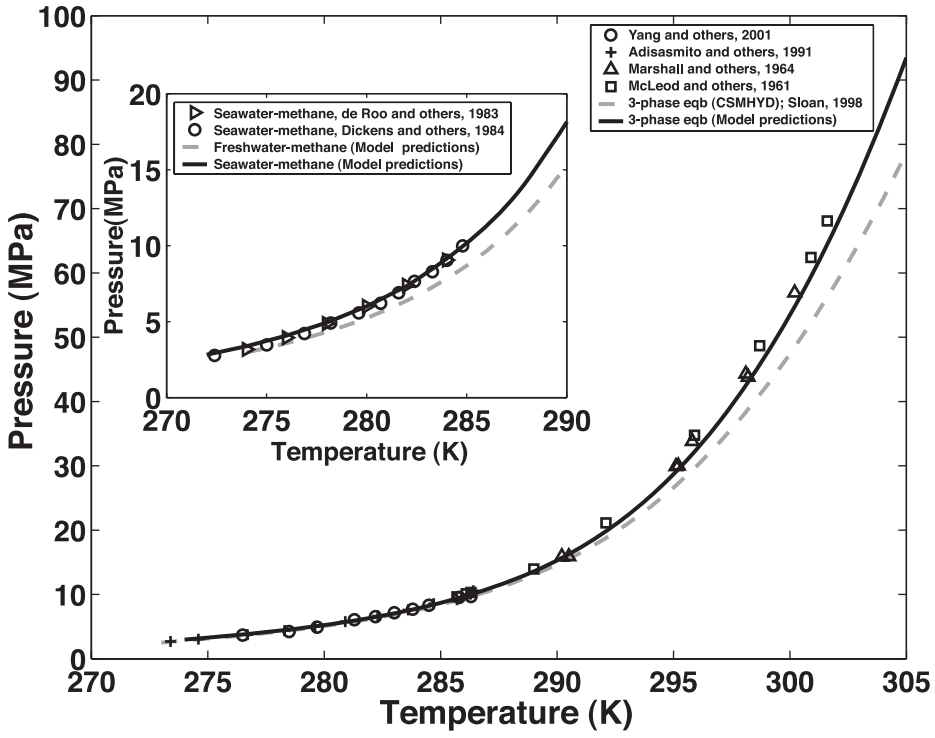

Fig. 2. Three-phase equilibrium curves for the methane-pure water system compared with results from CSMHYD (dashed curve) and experimental data. Inset shows experimental and calculated equilibrium curves for the methane-seawater (0.6m NaCl solution) system.

Seo and others, 2002). Several approaches for approximating methane solubility in the L-H region have been published (Servio and Engelzos, 2002; Davie and others, 2004; Tishchenko and others, 2005). We compute the solubility as follows:

- for a given temperature T, the three-phase equilibrium pressure is calculated as above (eq 5), a calculation which also yields the cage occupancies (θ_i);
- an equation of state (Duan and others, 1992) is used to determine the solubility of methane x_{CH_4} in equilibrium with vapor at the three-phase point.
- the formulation proposed by Handa (1990) is used to find methane solubility at pressure exceeding the three-phase equilibrium pressure for given temperature.

As two examples, we show the relationship between methane solubility and pressure at constant temperatures of 278.15 K and 290 K (fig. 3). Experimental data from Seo and others (2002) is shown for comparison. Importantly, peak methane solubility occurs at the three-phase equilibrium pressure. At lower pressures, methane solubility steadily rises with increasing pressure, while at higher pressures, methane solubility drops slightly with increasing pressure.

Overall Methane Solubility Curve

We now plot the contours of methane solubilities in the L-V and L-H regions along with the three-phase equilibrium curve (fig. 4), using the above approaches. All results shown henceforth are for water with an activity equivalent to that of a 0.6m NaCl solution (or standard seawater). As an example, we consider seafloor conditions

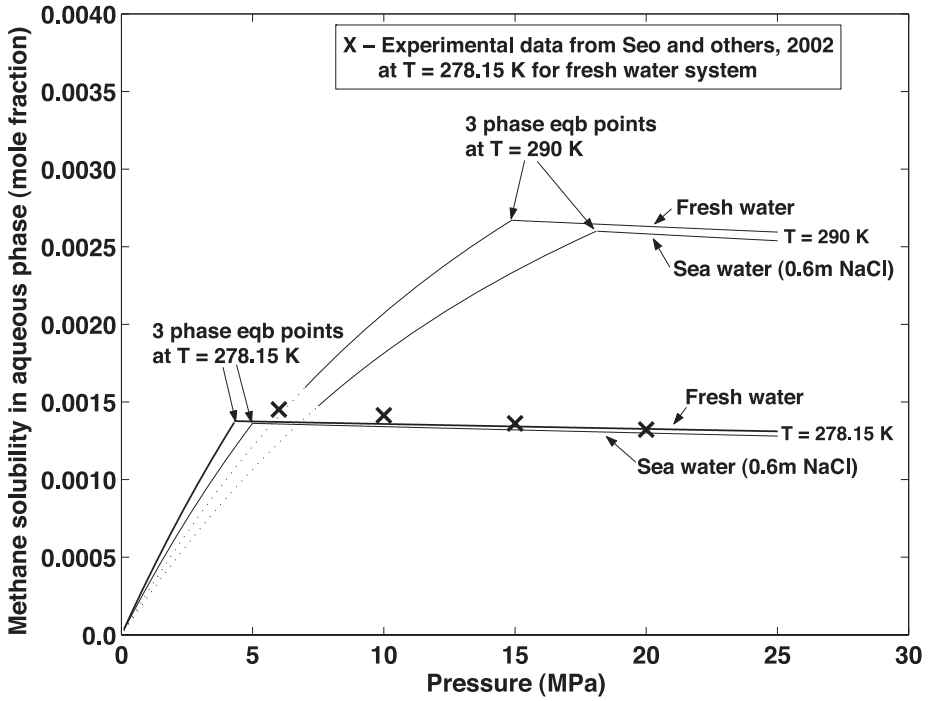

Fig. 3. Variation of methane solubility in aqueous phase with pressure in the L-V and L-H regions of the phase diagram at T = 278.15 K and T = 290 K, for methane-pure water and methane-seawater (0.6m NaCl solution) systems.

similar to those on the crest of outer Blake Ridge sediments (Paull and others, 1996): seafloor located at 2700 m below sea level (mbsl), seafloor temperature of 3 °C, and geotherm of 0.04 °C/m. For these conditions, the temperature profile within the sediments intersects the three-phase equilibrium curve at about 458 m below sea floor (mbsf), which marks the base of the GHSZ (fig. 4). Thus, provided methane is in excess of local solubility, gas hydrate can co-exist with the aqueous phase above 458 mbsf, whereas free gas can coexist with the aqueous phase below 458 mbsf.

Results from the contour plot can be combined into a single solubility curve (fig. 5) that forms the basis for understanding gas hydrate in marine sediments, where both pressure and temperature usually increase with depth. In general, methane solubility increases with depth within the GHSZ, reaches a local maximum at the base of the GHSZ and decreases slightly below. The specifics of the solubility curve depend on water depth, seafloor temperature, geothermal gradient and pore water salinity.

The vertical depth below the seafloor (fig. 5) can be normalized by the depth to the base of the GHSZ and denoted as L_t. Methane solubility can also be scaled with the peak concentration at this depth ($c^l_{m,eqb}$). This scaling fixes the base of the GHSZ at unit normalized depth with unit normalized methane solubility. The importance of this normalization will become evident later, when we discuss the sensitivity of hydrate saturation to changes in seafloor depth, seafloor temperature and geothermal gradient.

The phase stability and methane solubility curves are used to predict the amount and distribution of gas hydrate in marine sediment within a dynamic framework. We acknowledge a problem, however, with the use of constant water activity. Precipitation

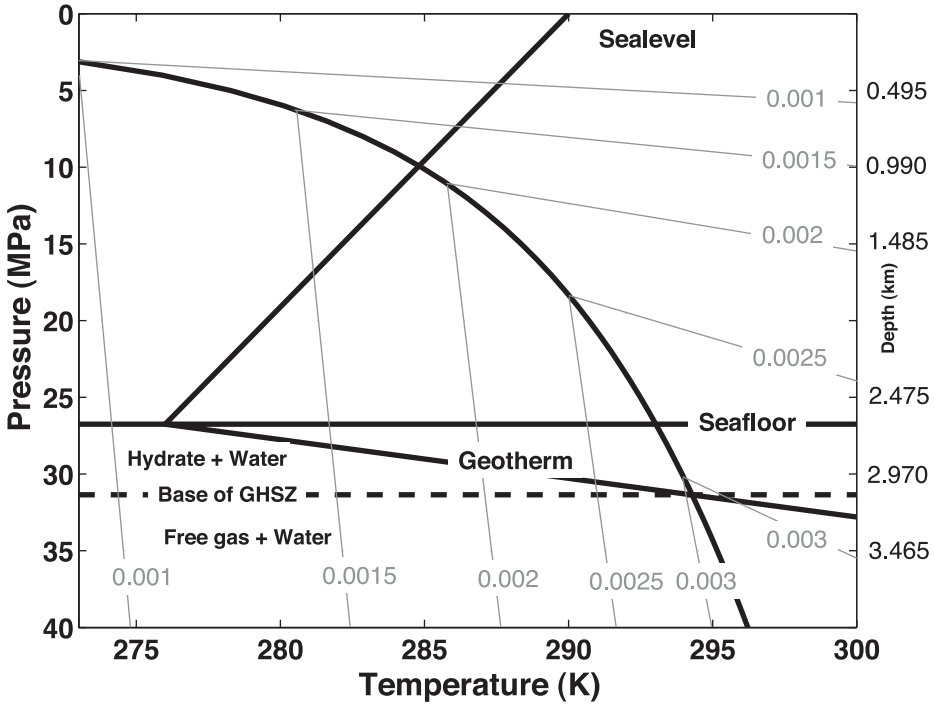

Fig. 4. Emergence of the GHSZ by imposing a seafloor depth, seafloor temperature and geothermal gradient on the solubility contour plot (mole fraction). The curve represents the three-phase seawater-methane equilibrium profile. A depth scale corresponding to hydrostatic pressure (assuming constant seawater density of 1030 kg/m^3) is plotted on the right axis to apply this phase diagram to a marine environment.

and dissociation of gas hydrate changes pore water salinity, which, in turn, impacts the phase boundaries and solubilities. We discuss effects of these changes later.

SEDIMENTATION AND COMPACTION

Sedimentation over geologic time scales leads to compaction of sediments. The theory of primary consolidation relates compaction and pore water expulsion to effective vertical stress (Terzaghi, 1943; Gibson, 1958). Constitutive relationships between porosity and effective vertical stress (Rubey and Hubbert, 1959) are used in many advanced compaction models that consider sedimentation on an impermeable basement in which the height of the seafloor above the basement becomes a dependent variable (Audet and Fowler, 1992; Wangen, 1992). The problem is essentially transformed into a moving boundary formulation, where the equations are more conveniently expressed in material derivative or Lagrangian form (Bethke, 1985).

For studying regional accumulation of gas hydrates, the primary issue is compaction driven flow in the upper few hundred meters of sediments. To simplify the problem mathematically, we set the reference frame at the seafloor, which is a standard approach used in modeling early diagenesis (Berner, 1980; Boudreau and Bennett, 1999). It is further assumed that depth is positive downwards, and pore pressure remains hydrostatic. Two additional assumptions are made for modeling fluid flow in the system:

- sediment and fluid densities remain constant
- sediment and fluid velocities become equal when minimum porosity is achieved

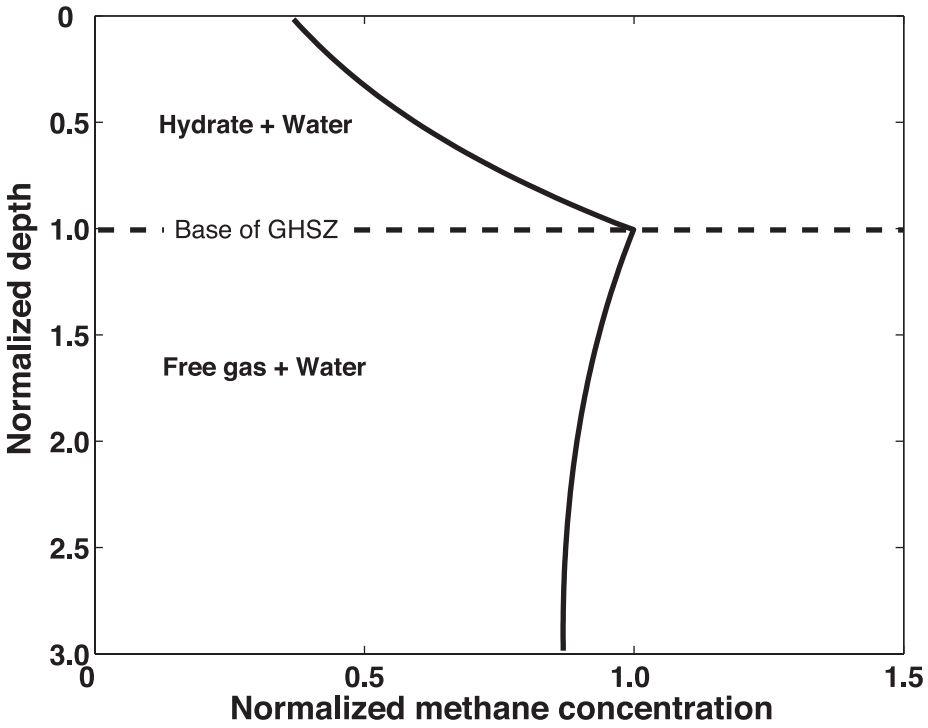

Fig. 5. Final methane solubility curve in a submarine setting obtained from the phase equilibrium and methane solubility calculations. The depth scale is scaled with respect to the depth of the base of the GHSZ and the methane concentration is scaled with the peak solubility at the base of the GHSZ.

We recognize two caveats to these assumptions. Pore pressures higher than hydrostatic may exist within gas hydrate systems (Flemings and others, 2003) and chemical diagenesis could change the component densities. These secondary effects are not incorporated in our first order model of regional processes.

For one-dimensional compaction (that is, zero lateral strain), porosity (ϕ) can be written as a function of the effective stress (σ_e), which is the difference between overburden (σ_v) and pore pressure (p) (Gibson, 1958; Rubey and Hubbert, 1959):

$$\phi = \phi_\infty + (\phi_0 - \phi_\infty) e^{-(\sigma_e/\sigma_\phi)} = \phi_\infty + (\phi_0 - \phi_\infty) e^{-(\sigma_v - p/\sigma_\phi)} \tag{6}$$

where σ_ϕ is a characteristic constant having units of stress, ϕ_0 is the porosity of sediments at the seafloor, and ϕ_∞ is the minimum porosity achieved. Taking the derivative of equation (6) and substituting expressions for the overburden and hydrostatic pore pressure yields:

$$-\sigma_\phi \left(\frac{\phi_0 - \phi_\infty}{\phi - \phi_\infty} \right) \frac{\partial}{\partial z} \left(\frac{\phi - \phi_\infty}{\phi_0 - \phi_\infty} \right) = (\rho_s - \rho_f)(1 - \phi) g \tag{7}$$

where z represents vertical depth, ρ_s and ρ_f denote sediment and fluid densities, respectively, and g represents acceleration due to gravity. Since σ_ϕ has units of stress, the term $\sigma_\phi / [(1 - \phi_\infty)(\rho_s - \rho_f) g]$ has units of length and can be used to non-dimensionalize the depth z. We define this term as the characteristic length L_ϕ, and the dimensionless depth $\tilde{z}$ as:

$$\tilde{z} = \frac{z}{L_\phi} = \frac{z}{\sigma_\phi/[(1-\phi_\infty)(\rho_s - \rho_f)\,g]} \tag{8}$$

The porosity at any given depth and the initial porosity can be rewritten in reduced form as follows:

$$\tilde{\phi} = \frac{\phi - \phi_\infty}{1 - \phi_\infty}, \quad \eta = \frac{\phi_0 - \phi_\infty}{1 - \phi_\infty} \tag{9}$$

where $\tilde{\phi}$ and η are reduced porosities at any given depth and at the seafloor, respectively. In terms of these reduced variables, equation (7) along with the boundary condition becomes:

$$\frac{1}{\tilde{\phi}}\frac{\partial\tilde{\phi}}{\partial\tilde{z}} = -(1-\tilde{\phi}),\ \text{B.C.: at } \tilde{z} = 0,\ \tilde{\phi} = \eta \tag{10}$$

Integration of equation (10) leads to the following analytical expression for reduced porosity as a function of dimensionless depth:

$$\tilde{\phi} = \frac{\eta}{\eta + (1-\eta)e^{\tilde{z}}} \tag{11}$$

A similar equation for porosity loss was derived by Boudreau and Bennett (1999). The porosity-depth relation (eq 11), along with mass balances for sediment and fluid phases, provides expressions for the flux of these phases (Berner, 1980; Davie and Buffett, 2001). The sediment balance can be written as:

$$\frac{\partial((1-\phi)\rho_s)}{\partial t} + \nabla\cdot(v_s\rho_s(1-\phi)) = 0 \tag{12}$$

where v_s is the sediment velocity. Assuming steady state leads to invariant sediment flux (U_s) with depth, which can be related to the sedimentation rate ($\dot{S}$) through the boundary condition imposed at the seafloor (Berner, 1980):

$$U_s = v_s(z)(1-\phi(z)) = [v_s(1-\phi)]_{\tilde{z}=0} = \dot{S}(1-\phi_0) \tag{13}$$

The fluid balance is shown later in the component balance section. As a closure for this system of equations it is generally assumed that fluid and sediment velocities approach a common asymptotic value as minimum porosity is achieved (Berner, 1980; Hutchison, 1985; Davie and Buffett, 2001). We make use of this assumption in our model and note that fluid velocity obtained from mass balances, in the absence of any external flux, is positive across all depths. This means that the fluid always moves downwards relative to the seafloor (Berner, 1980), and that transport of dissolved methane into the GHSZ by advection necessitates an upward external flux (Hyndman and Davis, 1992).

COMPONENT BALANCES AND GAS HYDRATE FORMATION

Methane Generation

Naturally occurring gas hydrates can derive their methane through two processes (Kvenvolden, 1993; Milkov, 2005). Decomposition of organic carbon buried with sediment can generate methane significantly faster than diffusion can remove it toward the seafloor. This could lead to "*in-situ*" precipitation of gas hydrate within the GHSZ (Paull and others, 1994; Egeberg and Dickens, 1999; Davie and Buffett, 2001). Advection of methane, either biogenic or thermogenic, from deeper sources can

supply methane into the GHSZ from below (Xu and Ruppel, 1999; Haeckel and others, 2004; Torres and others, 2004; Liu and Flemings, 2006). The progressive decrease of methane solubility with shoaling depth across the GHSZ (fig. 5) implies that gas hydrate can precipitate from methane charged fluids without requiring free gas (Hyndman and Davis, 1992). The development of a general model needs to consider gas hydrate accumulation from either of the two methane sources and from mixtures of both.

For *in-situ* methanogenesis, solid organic carbon buried with sediments ultimately provides the methane. Complete conversion of organic matter to methane proceeds via a series of complex reactions and pathways involving myriad compounds (Berner, 1980; Claypool and Kvenvolden, 1983; Whiticar and others, 1986; Wallmann and others, 2006). To simplify this process, we combine possible pathways for biogenic methane into a single first order reaction (Martens and Berner, 1977; Davie and Buffett, 2001). The rate of methane generation is assumed to be proportional to the available organic carbon present in the sediments and linked to it through a first order rate law. We acknowledge that in constructing a relatively general first-order model, we have neglected the complications arising from using such simple kinetics for organic decay. More advanced models for simulating organic decay and other coupled reactions have been recently published (Wallmann and others, 2006), but these introduce new parameters in the system, which makes our simulation results difficult to scale into simple plots.

Organic Material Balance for In-situ Production

The amount of organic carbon available to methanogens (α) is expressed as a mass fraction of total sediment. We note that α represents only a fraction of the total organic carbon (TOC) because not all can be converted to methane. The following assumptions are also made:

- sedimentation rate and the amount of degradable organic carbon at the seafloor (α_0) remain constant over time;
- microbial methanogenesis begins at the seafloor;
- solid organic material advects downwards with sediment velocity v_s;
- sediment density is not altered by microbial degradation of organic carbon.

The first two assumptions warrant brief discussion. Constant sedimentation rate and organic carbon supply are not valid over geologic time scales. This issue is addressed later. A sulfate reduction zone (SRZ) is present in shallow sediment above all gas hydrate systems examined to date (Borowski and others, 1999). The SRZ reduces the amount of TOC available for methanogenesis. More crucially, sulfate in pore water severely curtails methane production. Consequently, the SRZ shifts the zero methane boundary condition below the seafloor, often by 5 to 20 meters. Initial simulations indicate that the computational cost of resolving the thin SRZ far exceeds the change in average hydrate saturation it causes. We therefore neglect the SRZ in the model and simulations presented here.

With the above assumptions, the material balance for degradable organic carbon in one-dimension is (Berner, 1980; Davie and Buffett, 2001):

$$\frac{\partial}{\partial t}(\rho_s\alpha(1-\phi)) + \frac{\partial}{\partial z}(\rho_s v_s\alpha(1-\phi)) = -\rho_s\lambda\alpha(1-\phi) \tag{14}$$

where v_s is the sediment velocity, and λ is the first order rate constant. The initial and boundary conditions for this equation are:

$$\text{I.C.: } \alpha(z, 0) = 0 \tag{15}$$

$$\text{B.C.: } \alpha(0, t) = \alpha_0 \tag{16}$$

The equations and variables are now rewritten in dimensionless form to reduce the number of parameters describing the system. Defining dimensionless groups also helps to distinguish gas hydrate systems into separate categories, such as diffusion or advection dominated. The characteristic length of a gas hydrate system is better represented by the thickness of the GHSZ (L_t), rather than the length scale used in the sedimentation-compaction model. This depth (L_t) can be used to normalize the vertical depth in equation (14):

$$\tilde{z} = \frac{z}{L_t} \tag{17}$$

Further, the material balance can be written in terms of sediment and fluid fluxes instead of velocities. The degradable content of organic matter in the sediments is normalized with respect to its initial concentration at the seafloor (α_0). Time is non-dimensionalized by a combination of L_t and the methane diffusivity (D_m). The sediment flux (U_s) is non-dimensionalized with respect to the fluid flux caused by sedimentation ($U_{f,sed}$), which causes it to be equal to a constant, γ. The resulting non-dimensional variables are expressed as follows:

$$\tilde{\alpha} = \frac{\alpha}{\alpha_0} \tag{18}$$

$$\tilde{t} = \frac{t}{L_t^2/D_m} \tag{19}$$

$$\tilde{U_s} = \frac{U_s}{U_{f,sed}} = \frac{\dot{S}(1-\phi_0)}{U_{f,sed}} = \frac{\left(\frac{1-\phi_\infty}{\phi_\infty}\right)U_{f,sed}}{U_{f,sed}} = \frac{1-\phi_\infty}{\phi_\infty} = \gamma \tag{20}$$

The following important dimensionless groups can also be defined:

$$Da = \frac{\lambda L_t^2}{D_m} \tag{21}$$

$$Pe_1 = \frac{U_{f,sed} L_t}{D_m} \tag{22}$$

The Damkohler number (Da) represents the ratio of methanogenesis rate to methane diffusion. Higher values of Da imply higher methane production and/or lower methane diffusivity. The first Peclet number (Pe_1) is the ratio of fluid advection to methane diffusion. The use of Peclet and Damkohler numbers in modeling early diagenesis has been discussed in Boudreau (1997). The fluid flux used in defining Pe_1 denotes the contribution from sedimentation-compaction effects and will be supplemented by a second Peclet number, defined later, that will quantify the effect of upward external flow from deeper sources.

Using these dimensionless scalings, the organic mass balance (eq 14) can be rewritten as:

$$\frac{\partial}{\partial \tilde{t}}(\tilde{\alpha}(1-\tilde{\phi})) + Pe_1 \frac{\partial}{\partial \tilde{z}}\left(\frac{1+\gamma}{\gamma}\tilde{U_s}\tilde{\alpha}\right) = -Da(1-\tilde{\phi})\tilde{\alpha} \tag{23}$$

The initial and boundary conditions for the dimensionless organic material balance are:

$$\text{I.C.: } \tilde{\alpha}(\tilde{z}, 0) = 0 \tag{24}$$

$$\text{B.C.: } \tilde{\alpha}(0, \tilde{t}) = 1 \tag{25}$$

The porosity equation (11) was non-dimensionalized by a characteristic length L_ϕ, whereas the organic material balance equation (23) uses the GHSZ as a characteristic length. To use the same expression for porosity in the organic balance equation, we have to define another dimensionless group ($N_{t\phi}$) which is the ratio of these two characteristic lengths:

$$N_{t\phi} = \frac{L_t}{L_\phi} \tag{26}$$

The new porosity relation becomes:

$$\tilde{\phi}(\tilde{z}) = \frac{\eta}{\eta + (1 - \eta)e^{N_{t\phi}\tilde{z}}} \tag{27}$$

Methane Balance and Gas Hydrate Formation

We now develop equations for simulating gas hydrate and free gas accumulation at thermodynamic equilibrium by imposing methane solubility curves on methane concentration profiles. The basic assumption is that gas hydrate accumulates when dissolved methane concentration exceeds local solubility. In making this assumption, though, it is worth commenting on the morphology and local distribution of gas hydrate within marine sediments. Macroscopic specimens (>1 cm) of gas hydrate have been recovered from drill cores in many locations (Kvenvolden, 1993; Paull and others, 1996; Tréhu and others, 2003). However, analyses of pore water chemistry, sediment temperature and downhole logs suggest that most gas hydrate in marine sediment is disseminated between sediment grains, especially in systems where diffusion dominates, but that it dissociates during core recovery (Paull and others, 1996; Tréhu and others, 2003). We assume in our model that gas hydrate is disseminated within pore space and does not deform surrounding sediments.

The following assumptions are made in formulating the methane material balance:

- dissolved methane does not alter the fluid density, ρ_f
- a sulfate reduction zone is not present
- mass fraction of water in aqueous phase is unity due to low solubility of methane in pore water
- hydrate and free gas phases are immobile and move with sediment velocity, v_s
- water density is the same in gas hydrate and aqueous phases
- free gas phase contains no water

We denote methane mass fraction in pore fluid by c_m^l, in hydrate phase by c_m^h and in gas phase by c_m^g. The three-phase material balance can be written in one-dimension as:

$$\frac{\partial}{\partial t}[\phi(1 - S_h - S_g)\rho_f c_m^l + \phi S_h c_m^h \rho_h + \phi S_g c_m^g \rho_g] + \frac{\partial}{\partial z}\left[U_f c_m^l \rho_f + U_s \frac{\phi}{1 - \phi} S_h c_m^h \rho_h + U_s \frac{\phi}{1 - \phi} S_g c_m^g \rho_g\right] = \frac{\partial}{\partial z}\left[\phi(1 - S_h - S_g) D_m \rho_f \frac{\partial c_m^l}{\partial z}\right] + \frac{M_{CH_4}}{M_{org}} \rho_s \lambda (1 - \phi)\alpha \tag{28}$$

where ρ_f, ρ_h and ρ_g are densities of water, gas hydrate and free gas, respectively, S_h is the gas hydrate saturation in the pore space, S_g is the free gas saturation in the pore space, and M_{CH_4} and M_{org} are the molecular weights of methane and organic matter, respectively. The first expression on the left side gives the rate of accumulation of

methane in the aqueous, gas hydrate and free gas phases. The second term on the left side represents the flux of methane in the aqueous, gas hydrate and free gas phases. The first term on the right side characterizes the diffusion of methane in the pore fluid. The last term corresponds to the generation of methane through the first order organic reaction, and couples the methane mass balance to the organic mass balance in equation (23).

An initial condition and two boundary conditions are required to solve this partial differential equation. We specify zero initial methane concentration in the pore fluid, consistent with zero initial organic matter in sediment. A Dirichlet boundary condition corresponding to zero methane concentration at the seafloor is used along with a Neumann boundary condition of zero diffusive flux of methane at the bottom of the model (depth D). These conditions can be written as:

$$\text{I.C.: } c_m^l(z, 0) = 0 \tag{29}$$

$$\text{B.C. (1): } c_m^l(0, t) = 0 \tag{30}$$

$$\text{B.C. (2): } \frac{\partial c_m^l}{\partial z}(D, t) = 0 \tag{31}$$

We non-dimensionalize equation (28) using the same dimensionless groups and scalings for depth, organic content and time as defined previously (eqs 17–19). The methane mass fractions in the pore fluid (c_m^l), gas hydrate (c_m^h) and free gas phase (c_m^g) are normalized with the methane solubility at the base of the GHSZ. This value, denoted by $c_{m,eqb}^l$, is calculated from the phase equilibrium results for a given seafloor depth, temperature, geothermal gradient and pore water salinity. The scaled methane mass fractions are defined as:

$$\tilde{c}_m^l = \frac{c_m^l}{c_{m,eqb}^l},\ \tilde{c}_m^h = \frac{c_m^h}{c_{m,eqb}^l},\ \tilde{c}_m^g = \frac{c_m^g}{c_{m,eqb}^l} \tag{32}$$

The dimensionless form of the three-phase methane balance can be written as:

$$\begin{aligned}
&\frac{\partial}{\partial \tilde{t}}\left[\frac{1+\gamma\tilde{\phi}}{\gamma}(1-S_h-S_g)\tilde{c}_m^l + \frac{1+\gamma\tilde{\phi}}{\gamma}S_h\tilde{c}_m^h\tilde{\rho}_h + \frac{1+\gamma\tilde{\phi}}{\gamma}S_g\tilde{c}_m^g\tilde{\rho}_g\right] \\
&\quad + \frac{1+\gamma}{\gamma}\frac{\partial}{\partial \tilde{z}}\left[(Pe_1 + |Pe_2|)\tilde{U}_f\tilde{c}_m^l + Pe_1\tilde{U}_s\frac{(1+\gamma\tilde{\phi})}{\gamma(1-\tilde{\phi})}S_h\tilde{c}_m^h\tilde{\rho}_h + Pe_1\tilde{U}_s\frac{(1+\gamma\tilde{\phi})}{\gamma(1-\tilde{\phi})}S_g\tilde{c}_m^g\tilde{\rho}_g\right] \\
&\quad = \frac{\partial}{\partial \tilde{z}}\left[\frac{1+\gamma\tilde{\phi}}{\gamma}(1-S_h-S_g)\frac{\partial \tilde{c}_m^l}{\partial \tilde{z}}\right] + \left(\frac{M_{CH_4}\rho_s}{M_{org}\rho_f}\right)Da(1-\tilde{\phi})\beta\tilde{\alpha},
\end{aligned} \tag{33}$$

where Pe_2 is defined in the next section, $\tilde{\rho}_h$ is the ratio of hydrate to fluid density, $\tilde{\rho}_g$ is the ratio of free gas and fluid density, and β is the normalized initial organic carbon content at the time of deposition, defined as:

$$\tilde{\rho}_h = \frac{\rho_h}{\rho_f},\ \tilde{\rho}_g = \frac{\rho_g}{\rho_f} \tag{34}$$

$$\beta = \frac{\alpha_0}{c_{m,eqb}^l} \tag{35}$$

The values of c_m^h and $\tilde{\rho}_h$ are assumed to be constant and equal to 0.134 and 0.9, respectively, (table 1). Free gas density (ρ_g) is computed from the ideal gas law. Molecular weights M_{CH_4} and M_{org} are taken to be 16 and 30, respectively, while the ratio

ρ_s/ρ_f is set to 2.65/1.03 = 2.57 (table 1). The dimensionless initial and boundary conditions become:

$$\text{I.C.: } \tilde{c}^{\,l}_m(\tilde{z}, 0) = 0 \tag{36}$$

$$\text{B.C. (1): } \tilde{c}^{\,l}_m(0, \tilde{t}) = 0 \tag{37}$$

$$\text{B.C. (2): } \frac{\partial \tilde{c}^{\,l}_m}{\partial \tilde{z}}(D, \tilde{t}) = 0 \tag{38}$$

External Upward Fluid Flow and Water Balance

In gas hydrate settings where *in-situ* methanogenesis provides all methane, the fluid flux will be dominated by that resulting from compaction ($U_{f,sed}$). However, to incorporate the possibility of a deep methane source, an external fluid flux is required. We thus superimpose an external flux (U_{ext}) on the flux caused by compaction ($U_{f,sed}$) to get a total flux (U_f), as described by Davie and Buffett (2003b):

$$U_f = U_{f,sed} + U_{ext} \tag{39}$$

Since the depth variable is taken to be positive downwards, the flux due to sedimentation remains positive. However, the external flux U_{ext} is directed upwards and will have a negative value. If U_{ext} exceeds $U_{f,sed}$ in magnitude, the net flux will be negative, and fluid flow will be toward the seafloor. Alternatively, if the magnitude of U_{ext} is less than $U_{f,sed}$, the net flux will be positive and fluid flow will be down. In case of equal magnitudes, U_f will be zero and methane transport will occur through diffusion only.

The total fluid flux is used as a boundary condition when solving the water mass balance, which can be written as:

$$\frac{\partial}{\partial t}\left[\phi S_w c^{\,l}_w \rho_f + \phi S_h c^{\,h}_w \rho_h\right] + \frac{\partial}{\partial z}\left[U_f c^{\,l}_w \rho_f + U_s \frac{\phi}{1-\phi} S_h c^{\,h}_w \rho_h\right] = 0 \tag{40}$$

where $c^{\,l}_w$ and $c^{\,h}_w$ are water mass fractions in the aqueous and hydrate phases, respectively, and S_w is water saturation ($S_w = 1 - S_h - S_g$). The assumption of negligible methane solubility in water makes $c^{\,l}_w$ approximately equal to unity. Further, the assumption of constant water density in the aqueous and hydrate phases makes the term $[\phi S_w c^{\,l}_w \rho_f + \phi S_h c^{\,h}_w \rho_h]$ invariant over time and drives the first term on the left side of equation (40) to zero. This assumption helps to decouple the water and methane mass balances, so that they do not have to be solved simultaneously. Equation (40) can be rewritten as:

$$\frac{\partial}{\partial z}\left[U_f + U_s \frac{\phi}{1-\phi} S_h c^{\,h}_w \tilde{\rho}_h\right] = 0 \Rightarrow U_f + U_s \frac{\phi}{1-\phi} S_h c^{\,h}_w \tilde{\rho}_h = const. \tag{41}$$

As long as no hydrate forms in the system, the flux of water in the aqueous phase is constant and equal to the total fluid flux. Once hydrate starts to accumulate in pore space, water moves into the hydrate phase and the flux of water in the aqueous phase decreases. We make use of the total flux at $\tilde{z} = 0$ as a boundary condition by rewriting equation (41) as:

$$U_f + U_s \frac{\phi}{1-\phi} S_h c^{\,h}_w \tilde{\rho}_h = \left(U_f + U_s \frac{\phi}{1-\phi} S_h c^{\,h}_w \tilde{\rho}_h\right)_{\tilde{z}=0} \tag{42}$$

The hydrate saturation at $\tilde{z} = 0$ is always zero due to the boundary condition on dissolved methane (eq 37). This enables us to rewrite equation (42) as:

$$U_f + U_s \frac{\phi}{1-\phi} S_h c^{\,h}_w \tilde{\rho}_h = (U_f)_{\tilde{z}=0} = U_{f,sed} + U_{ext} \tag{43}$$

which can be rearranged to:

$$U_f = U_{f,sed} + U_{ext} - U_s \frac{\phi}{1-\phi} S_h c_w^h \tilde{\rho}_h \tag{44}$$

To develop the most general model applicable for all cases, such as zero sedimentation, zero external flux or zero net flux ($|U_{f,sed}| = |U_{ext}|$), we normalize equation (44) by the sum ($U_{f,sed} + |U_{ext}|$). Equation (44) can then be cast as:

$$\tilde{U}_f = \frac{U_f}{U_{f,sed} + |U_{ext}|} = \frac{U_{f,sed} + U_{ext}}{U_{f,sed} + |U_{ext}|} - \frac{U_s}{U_{f,sed} + |U_{ext}|} \frac{\phi}{1-\phi} S_h c_w^h \tilde{\rho}_h \tag{45}$$

Multiplying numerators and denominators by the term (L_t/D_m), and making use of the definition of Peclet numbers, the fluid flux in dimensionless form is given by:

$$\tilde{U}_f = \left[\frac{Pe_1 + Pe_2}{Pe_1 + |Pe_2|}\right] - \frac{Pe_1 \tilde{U}_s}{Pe_1 + |Pe_2|} \frac{(1 + \gamma\tilde{\phi})}{\gamma(1-\tilde{\phi})} S_h c_w^h \tilde{\rho}_h \tag{46}$$

$$Pe_2 = \frac{U_{ext} L_t}{D_m} \tag{47}$$

where Pe_2 is a second Peclet number corresponding to the ratio of external flux to diffusion. Thus, our numerical model has two independent Peclet numbers that characterize the compaction-driven and external fluxes with respect to diffusion. Importantly, Pe_1 will be positive, whereas Pe_2 will be negative so that fluid flux due to sedimentation dominates when $|Pe_2| < |Pe_1|$ and external flux dominates when $|Pe_2| > |Pe_1|$.

For cases where external fluid flux dominates, the methane concentration in rising fluids needs specification. This methane concentration, denoted by $c^l_{m,ext}$, is imposed as a Dirichlet boundary condition at the bottom of the domain, replacing the Neumann boundary condition in equation (38). It is normalized as:

$$\tilde{c}^l_{m,ext} = \frac{c^l_{m,ext}}{c^l_{m,eqb}} \tag{48}$$

$$\text{B.C. (2): } \tilde{c}^l_m(D, \tilde{t}) = \tilde{c}^l_{m,ext}, \quad \text{for } |Pe_2| > |Pe_1| \tag{49}$$

NUMERICAL SOLUTION

Organic Carbon Balance

We first show the evolution of organic content within sediments (fig. 6) by numerically solving the organic mass balance (eq 23). This hyperbolic partial differential equation can be solved independently of the methane material balance (eq 33). We compute the numerical solution in conservative form using an implicit block-centered finite difference scheme. A single point upstream weighting was used for the advection term. All results shown henceforth are for the following parameters: $\eta = 6/9$, $\gamma = 9$, $N_{t\phi} = 1$. These values correspond to seafloor porosity $\phi_0 = 0.7$ and minimum porosity $\phi_\infty = 0.1$ (table 1).

The profile of "available" organic matter in sediment depends on the ratio Pe_1/Da, which given above (eqs 21 and 22), signifies the ratio of sedimentation to methanogenesis. In general, the organic content decreases with depth because of microbial decomposition during burial (fig. 6). Moreover, as the ratio Pe_1/Da increases, sedimentation increases with respect to methanogenesis, which means a higher carbon input at the seafloor or a lower reaction rate. Solid organic carbon available for methanogenesis reaches greater sediment depths with higher Pe_1/Da.

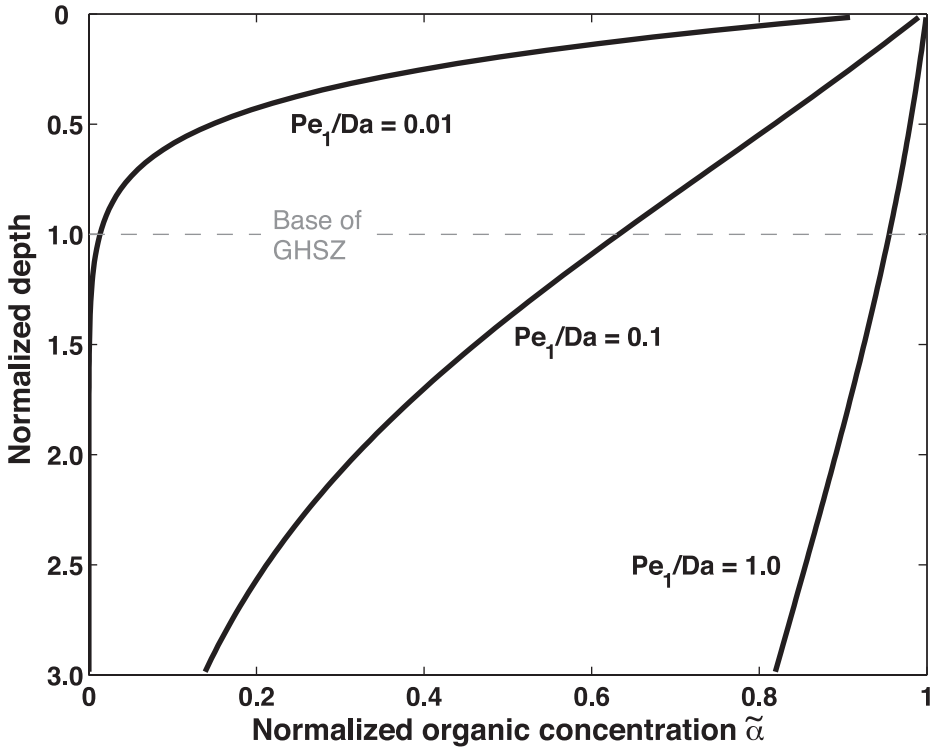

Fig. 6. Normalized organic concentration profiles at steady state as a function of the ratio Pe_1/Da. Lower values of Pe_1/Da lead to lesser organic content leaving the GHSZ, resulting in higher methane generation within the GHSZ.

Methane Mass Balance

To simulate gas hydrate accumulation in marine sediment, mass balances for methane and water are solved numerically. The solution to the methane balance partial differential equation (33) is computed in finite difference form after updating the organic content profile in time. Solution of the equations in conservative form ensures that there are no local material balance errors (all simulations had material balance errors less than 10^{-12}).

The methane mass balance equation contains three unknowns, $\tilde{c}_m^l$, S_h and S_g, which must be solved at each time step. This apparently under-determined system can be solved, however, by realizing that all three cannot be the primary dependent variable at any given time. As long as the methane concentration in pore fluid is lower than the local solubility, $\tilde{c}_m^l$ is the primary variable and the saturations S_h and S_g are zero. Once dissolved methane exceeds solubility conditions within the GHSZ, $\tilde{c}_m^l$ is set equal to the solubility, and excess methane goes into the hydrate phase. In this case, S_g is set to zero, and S_h becomes the primary dependent variable. Alternatively, when dissolved methane exceeds solubility conditions below the GHSZ, $\tilde{c}_m^l$ is again set equal to the solubility, but excess methane goes into free gas. In this case, S_h is set equal to zero, and S_g becomes the primary dependent variable. Importantly, any gas hydrate crossing the base of GHSZ dissociates to dissolved methane, which can become free gas provided pore fluid is already saturated with methane. These checks for switching among $\tilde{c}_m^l$, S_h and S_g as the primary dependent variable are done at each grid-block for each time-step of the simulations.

RESULTS AND DISCUSSION

In-situ Methanogenesis

The simplest case of methane accumulation to consider is *in-situ* methane generation with no external fluid flux. Transient profiles of dissolved methane concentration and gas hydrate and free gas saturation can be obtained from numerical simulations (fig. 7). Most simulations reach steady state within 2 to 3 units of dimensionless time ($\tilde{t}$). For $L_t \approx 450$ mbsf (similar to Blake Ridge; Paull and others, 1996) and $D_m = 10^{-9}$ m^2/s (Davie and Buffett, 2001), steady state is achieved within approximately 12 Myr. This "residence time" is similar to that predicted from other mass balance calculations (Davie and Buffett, 2001; Dickens, 2003).

Simulations (fig. 7) follow a common path toward steady state. Initially, there is no gas hydrate in pore space because dissolved methane concentrations are less than local solubility. When methane concentrations reach the solubility curve, gas hydrate starts to precipitate. With additional methane supply and sediment burial, the fraction of gas hydrate in sediment increases, and the lowermost occurrence of gas hydrate progressively moves down. In most cases, gas hydrate, when formed, reaches the base of the GHSZ after sufficient time. Gas hydrate dissociates upon crossing this horizon, generating free gas. Hence, at steady state there is a free gas layer immediately below gas hydrate (Davie and Buffett, 2001).

For both transient and steady state simulations, a series of gas zones can exist (fig. 7): an uppermost zone with dissolved methane, an intermediate zone with dissolved methane and gas hydrate, and a lower zone with dissolved methane and free gas. However, the presence and thickness of these gas zones can vary. A more interesting case occurs with a modest reduction in the initial organic content of the sediments (β). At relatively low β, depending on values for other parameters, a steady state can develop where gas hydrate does not extend to the base of the GHSZ, and free gas does not form below the GHSZ (fig. 8). Essentially, methane concentrations are less than the solubility curve starting at some depth above the base of the GHSZ.

Xu and Ruppel (1999) have suggested that this case arises when methane supply from depth does not exceed a critical flux. Our simulations show that this situation can also occur when modest organic carbon input does not furnish enough methane to saturate pore waters. Hence, a critical β has to be exceeded, analogous to the critical flux defined by Xu and Ruppel (1999), for hydrate and gas to coexist at the base of GHSZ.

Upward Methane Flux

Gas hydrate accumulation can also be simulated for systems where all methane is supplied from deeper sources and β is zero (fig. 9). As seen from transient profiles, methane enters the system from below and forms gas hydrate within the GHSZ when methane concentrations exceed solubility conditions. The gas hydrate layer then grows downwards because of sedimentation. At steady state, gas hydrate extends to the base of the GHSZ and free gas forms below.

A certain minimum methane flux is required to form gas hydrate in this case. However, a critical methane flux from below is not required for gas hydrate to contact free gas at the base of the GHSZ. Assuming constant methane supply and sufficient time, once hydrate has precipitated, a gas hydrate/free gas interface will occur even at relatively low methane fluxes because sedimentation moves gas hydrate towards the base of the GHSZ. If we do not include sedimentation effects in our model by setting Pe_1 to zero, as done by Xu and Ruppel (1999), the hydrate phase becomes immobile within the sediments and we also observe the emergence of a critical flux required to

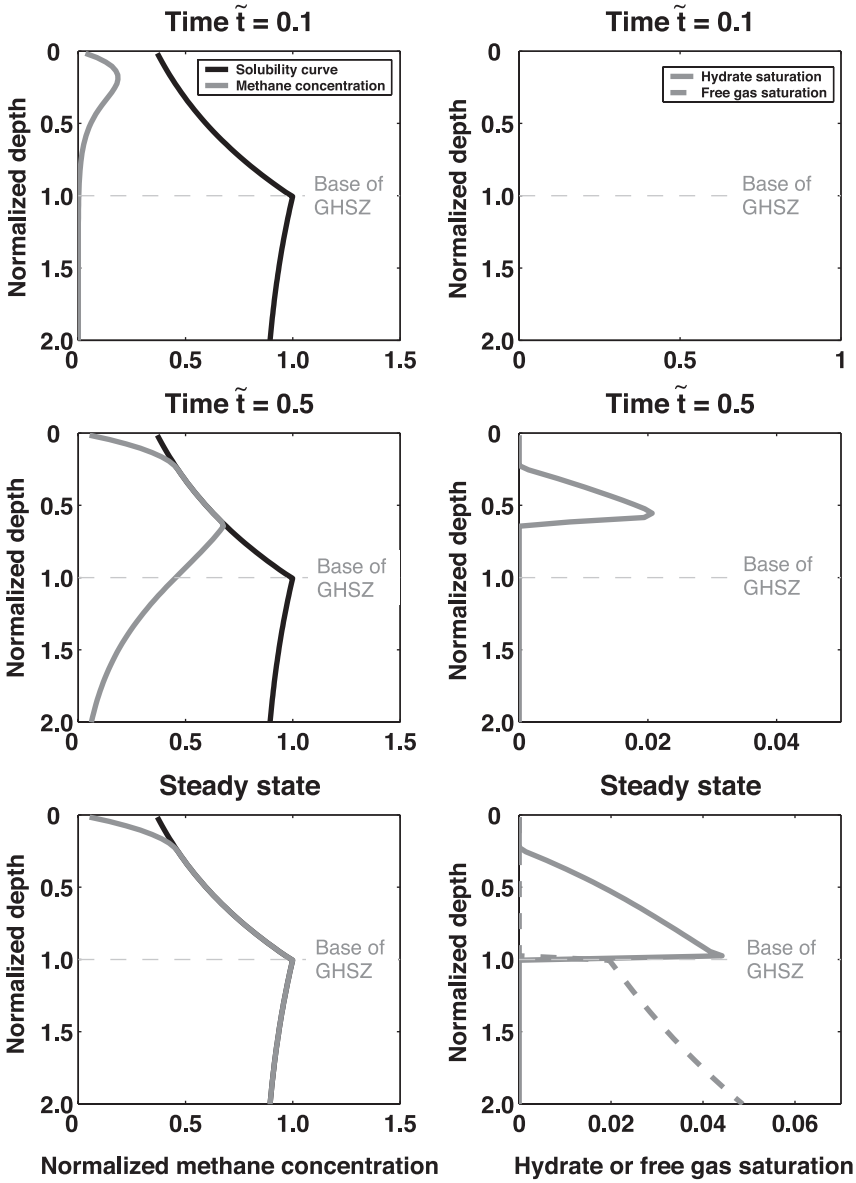

Fig. 7. Simulations showing the time evolution of the dissolved methane concentration (left column) and the gas hydrate and free gas saturation in the sediments (right column). The results shown above are for methane generated from biogenic *in-situ* sources only. A finite gas hydrate layer along with a free gas layer exists at steady state. The following model parameters were used for this simulation: $Pe_1 = 0.1$, $Da = 10$, $\beta = 3$, $Pe_2 = 0$, $\eta = 6/9$, $\gamma = 9$. The seafloor parameters used are for the Blake Ridge area: Seafloor depth = 2700 m, seafloor temperature = 3 °C and geothermal gradient = 0.04 °C /m. We refer to these seafloor parameters as the base case values.

bring the hydrate and free gas layers together at the base of the GHSZ (fig. 10). The methane solubility below the GHSZ was assumed to be constant for comparison with the results of Xu and Ruppel (1999). It can be seen that the critical flux needed for the hydrate and free gas phases to coexist at the base of the GHSZ is $Pe_2 \approx -5$.

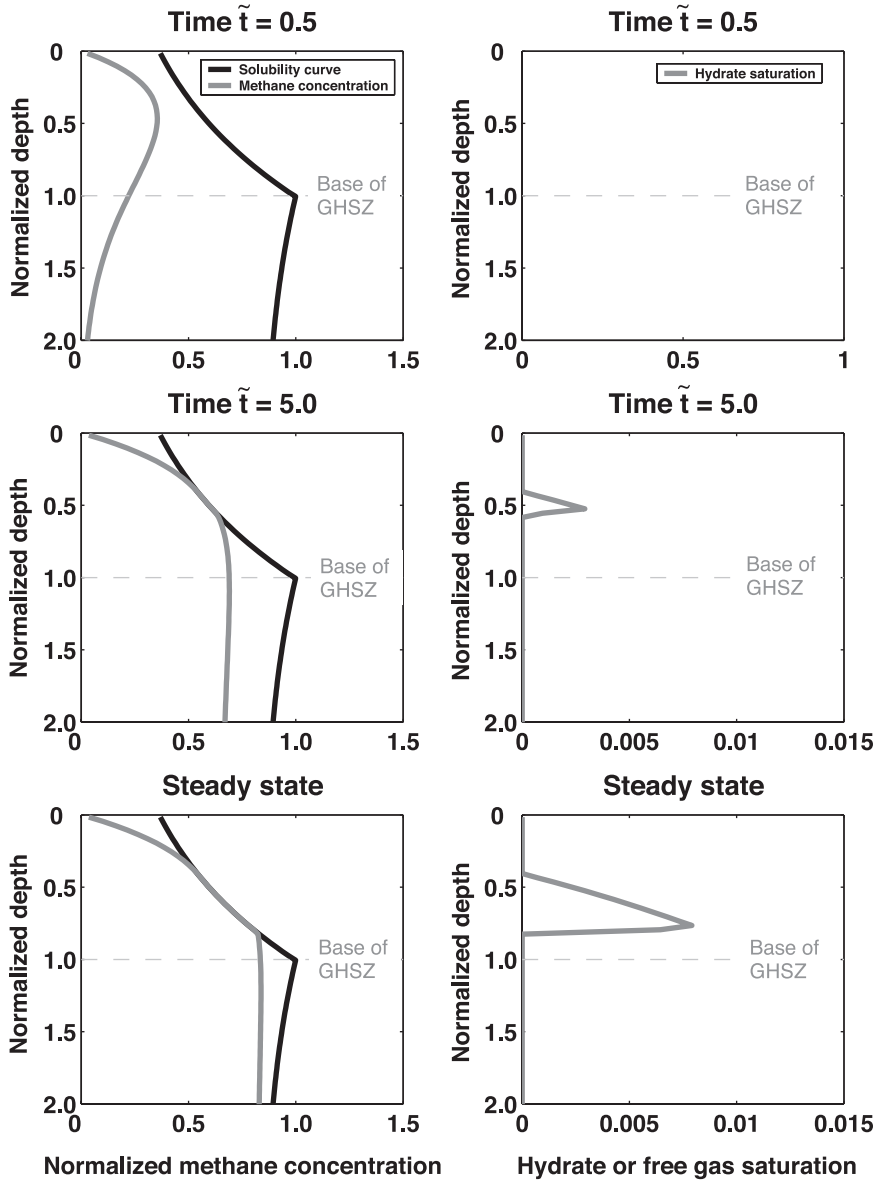

Fig. 8. Simulations showing the time evolution of methane concentration and gas hydrate saturation (similar to fig. 7), except that this system has a smaller value of β, resulting in lesser carbon input. This causes an isolated hydrate layer to exist at steady state, without any free gas below. The following model parameters were used for this simulation: $Pe_1 = 0.1$, $Da = 10$, $\beta = 1.4$, $Pe_2 = 0$, $\eta = 6/9$, $\gamma = 9$. Base case seafloor parameters were used for this simulation.

Combined Systems (Both Sources)

Gas hydrate systems with *in-situ* methanogenesis providing all methane can be simulated by setting $Pe_2 = 0$; those where rising fluids supply all methane can be studied by setting $\beta = 0$. Gas hydrate systems with mixed sources of methane can be simulated by assuming non-zero values of these parameters. General analysis of these systems,

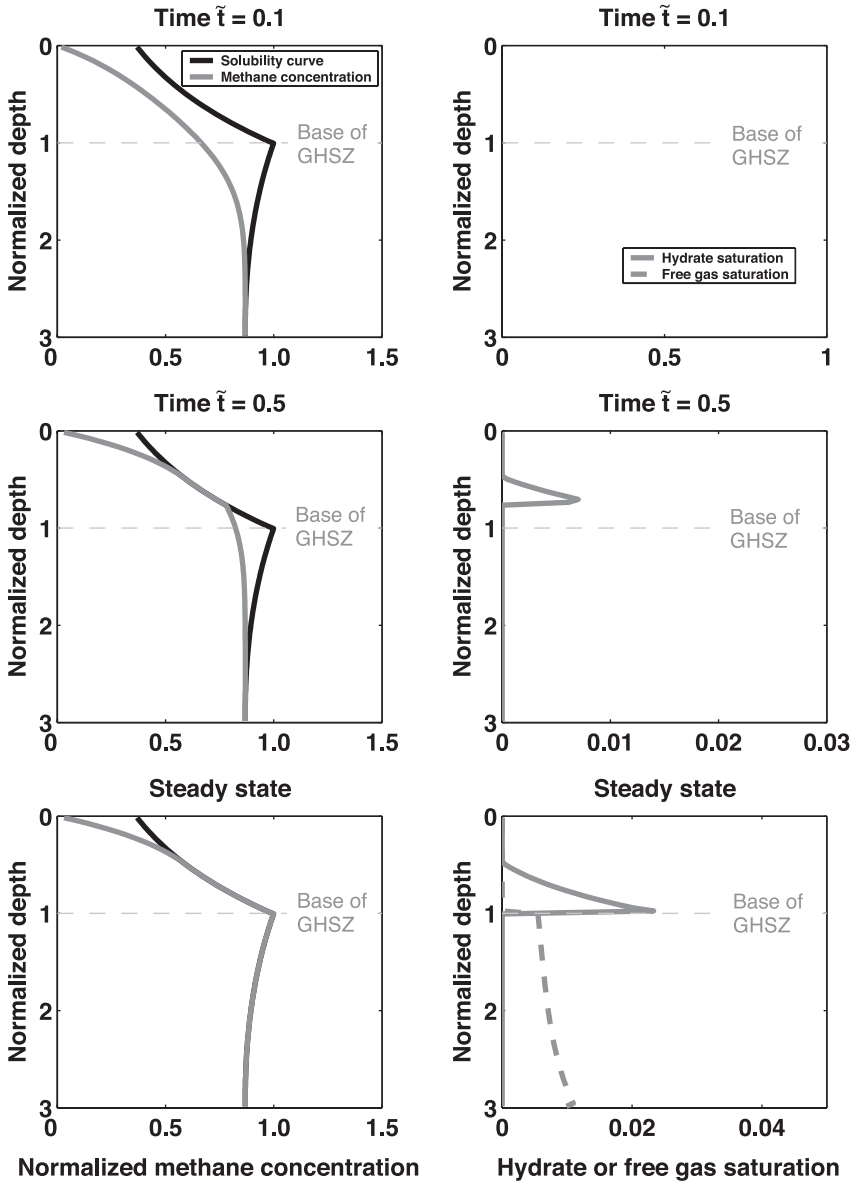

Fig. 9. Simulations showing the time evolution of methane concentration and gas hydrate and free gas saturation (similar to figs. 7 and 8), except that the methane in this case is transported by an upward external flux from a deeper source. A gas hydrate layer exists at steady state, with free gas below. The following model parameters were used for this simulation: $Pe_1 = 0.1$, $Da = 0$, $\beta = 0$, $Pe_2 = -2.0$, $\tilde{c}_{m,ext} = 0.9$, $\eta = 6/9$, $\gamma = 9$. Base case seafloor parameters were used for this simulation.

however, is complicated due to the large number of independent parameters. Thus, in the following two sections, we examine how changes in various parameters affect the behavior of these two end member systems.

Generalized Methanogenic Systems

The simulations of gas hydrate systems considered so far (figs. 7, 8 and 9) pertain to particular sets of parameter values. To obtain a more general understanding,

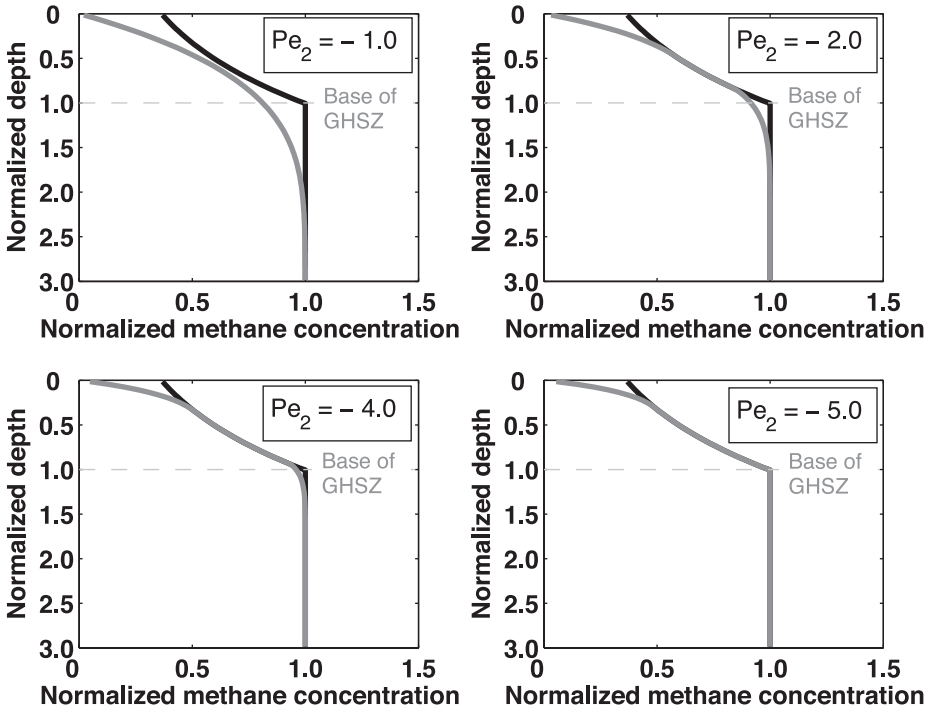

Fig. 10. Steady state dissolved methane concentration profiles for the case of methane supplied from deeper sources and without the effect of sedimentation ($Pe_1 = 0$). As Pe_2 increases in magnitude (that is, upward external flux becomes more important), the gas hydrate and free gas layers approach each other and co-exist at the base of the GHSZ only if the critical flux $Pe_2 = -5.0$ is exceeded. Parameters used for these simulations are: $Pe_1 = 0$, $\tilde{c}_{m,ext} = 1.0$, Pe_2 varies for the four plots. Base case seafloor parameters were used for this simulation.

numerous simulations can be performed for a range of parameters. For systems dominated by *in-situ* methanogenesis, sensitivity analyses reveal that Pe_1, Da and β dominantly affect the distribution of gas hydrate and free gas (Davie and Buffett, 2001; Buffett and Archer, 2004).

If Da is constant, the general distribution of hydrate at steady state in terms of β and Pe_1 can be divided into three fields (fig. 11). These fields define conditions where gas hydrate will occur, and with or without free gas at the base of the GHSZ. Paths can be followed across the fields to understand how parameters affect gas hydrate systems. For example, consider a path of constant Pe_1 (fig. 11): there is no gas hydrate at low β, gas hydrate without underlying free gas at intermediate β, and gas hydrate with free gas below the GHSZ at high β. The separation of these three fields at relatively low Pe_1 can be understood by realizing that, at low Pe_1, the system is dominated by high rates of diffusion, which causes loss of methane from the seafloor. To compensate for this loss, the burial of organic carbon at the seafloor and production of methane has to increase to accumulate gas hydrates.

As Pe_1 increases, one might expect gas hydrates to form at progressively lower values of β. However, this inverse relationship does not occur when Pe_1 exceeds about 0.6. Instead, the system requires more organic carbon (higher β) to form gas hydrates (fig. 11). This effect results from the increase in sediment velocity associated with the increase in Pe_1. Essentially, organic carbon moves through the GHSZ faster, and

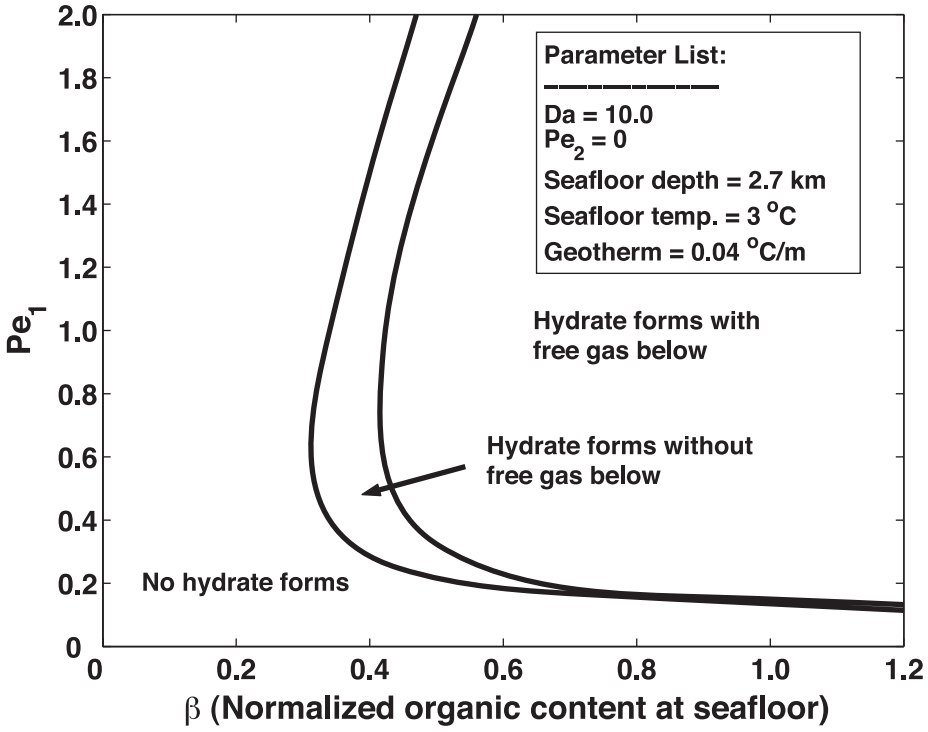

Fig. 11. Parameter space of Pe_1 and β showing three different fields of gas hydrate distribution. As β increases, with Pe_1 held constant, the system moves from the state of no gas hydrate to gas hydrate without free gas below and finally to gas hydrate with free gas below.

because the Damkohler number is fixed, greater amounts of organic carbon leave the GHSZ unreacted (fig. 6).

The relationship between Pe_1, Da and β can be explored further by realizing that the ratio Pe_1/Da controls organic decay and subsequent methane generation. Instead of keeping Da constant, therefore, the three distinct regions of gas hydrate distribution can be examined for constant Pe_1/Da (fig. 12). Again, there are three regions: there is a region of no hydrate formation at low β, a narrow central region of hydrate without associated free gas at moderate β, and a region corresponding to hydrate with free gas below at high β. This representation serves two purposes. First, curves representing gas hydrate formation and accumulation steadily decrease in Pe_1 as β gradually increases. The parameter space is, therefore, divided into two main regions: diffusion dominated at low Pe_1 and advection dominated at higher Pe_1. Second, the dependence of hydrate distribution on the Damkohler number can be included in the results explicitly.

Ideally, single plots can summarize the dependence of gas hydrate systems upon all relevant parameters. For *in-situ* methanogenesis, this can be achieved by realizing that each set of curves (fig. 12) represents different amounts of organic carbon conversion; that is, the quantity that binds different curves together is the amount of organic carbon converted within the GHSZ. At steady state, this quantity can be obtained from the normalized organic content at the base of the GHSZ. The analytical solution to the organic mass balance equation (eq 23, at $\tilde{z} = 1$) is:

$$\tilde{\alpha}\big|_{\tilde{z}=1} = [\eta + (1-\eta)e^{N_{t\phi}}]^{-1/N_{t\phi}(1+\gamma)Pe_1/Da} \tag{50}$$

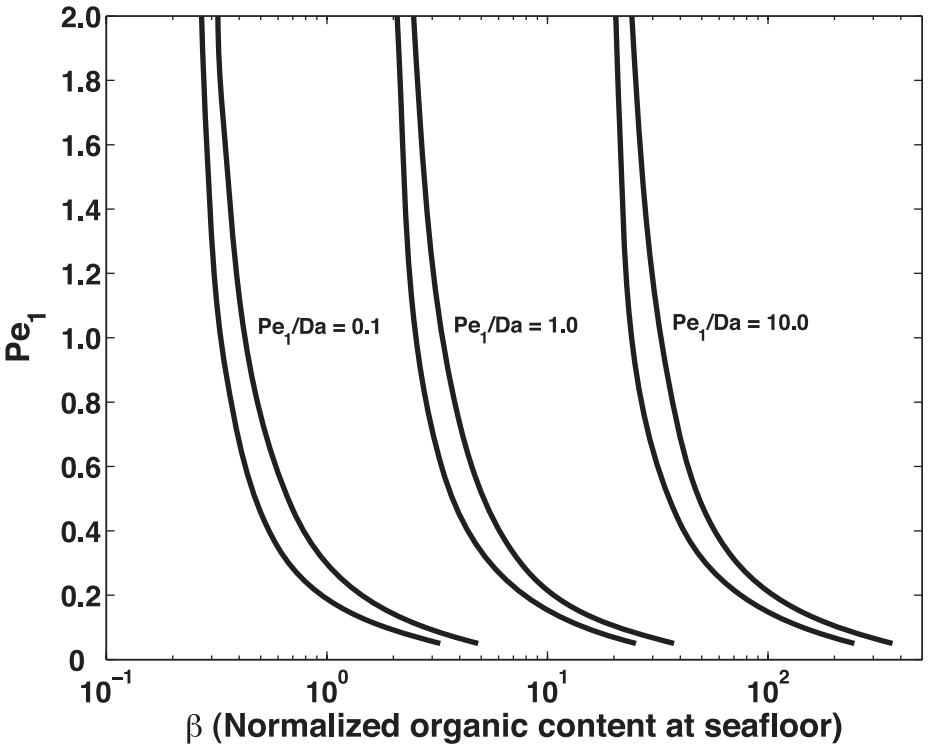

Fig. 12. Different gas hydrate regimes simulated for various ratios of Pe_1/Da. The region to the left of each pair of curves represents no gas hydrate formation, the narrow central region bounds the part where gas hydrate occurs without free gas below, and to the right of each pair is the region where gas hydrates occur with free gas below. Base case seafloor parameters were used for this simulation and $Pe_2 = 0$.

The amount of organic carbon converted within the GHSZ can be computed from this value and the carbon input at the seafloor (β):

$$\text{Amount of organic carbon converted in GHSZ} = (1 - \tilde{\alpha}|_{\tilde{z}=1})\beta \qquad (51)$$

If the curves shown in figure 12 for different values of Pe_1/Da are rescaled and plotted in figure 13, with the x-axis now representing the amount of organic carbon converted within the GHSZ (eq 51), we see that the different set of curves approximately collapse into one single pair of curves. The curves in figure 12 covered ratios of Pe_1/Da that were two orders of magnitude different. We are now able to summarize the dependence of gas hydrate distribution over a wide range of the relevant parameters (Pe_1, Da, β) with just one plot. This clearly highlights the importance of scaling the system by choosing appropriate dimensionless groups and variables.

Generalized Deeper Methane Systems

A simple, generalized plot can also be constructed for systems where all methane derives from deeper sources. The most important parameters in this case are the methane concentration in the upward migrating fluid ($\tilde{c}_{m,ext}$), Pe_1 and Pe_2. Deeper methane sources come into effect only when $|Pe_2| > |Pe_1|$.

We first examine results for different values of Pe_2 in the parameter space of Pe_1 and $\tilde{c}_{m,ext}$ (fig. 14). As mentioned before, we do not see the emergence of a zone of gas hydrate formation without free gas below at steady state for this type of source. Hence,

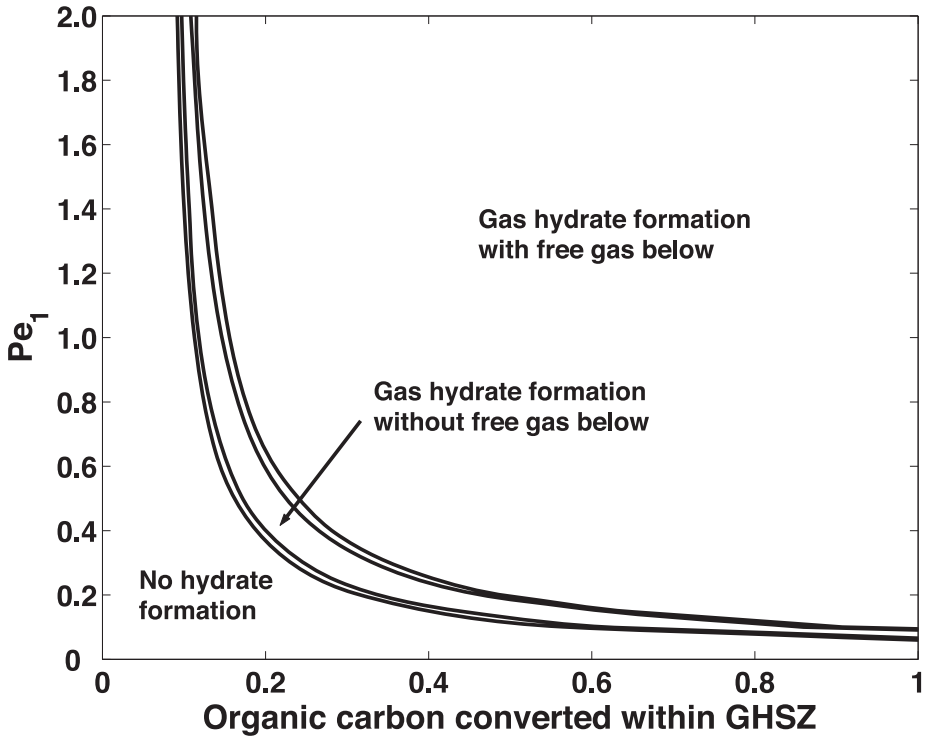

Fig. 13. Curves shown in figure 12 approximately collapse into a single pair of curves by rescaling and plotting them in a manner such that the x-axis represents the amount of organic carbon converted within the GHSZ (eq 51). Base case seafloor parameters were used for this simulation and $Pe_2 = 0$.

there is only one curve for each value of Pe_2, which separates parameters defining no gas hydrate formation from parameters defining gas hydrate with underlying free gas. Lower values of Pe_1 represent diffusion dominated systems, whereas higher values of Pe_1 describe systems dominated by advection. In the latter case, diffusive losses of methane are reduced, requiring less dissolved methane in the external flux. Increasing the external fluid flux $|Pe_2|$, keeping Pe_1 constant, implies greater net methane input to the system, thus requiring less $\tilde{c}_{m,ext}$ in the external flux to form gas hydrates.

To combine these multiple curves, we realize that net fluid flux is the controlling factor. If we rescale the parameter space so that the y-axis represents the net fluid flux in the system (algebraic sum of Pe_1 and Pe_2), the multiple curves for different Pe_2 collapse into a single curve (fig. 15). Thus, the entire parameter space for methane supplied from deeper sources can also be defined in a single plot.

Gas Hydrate Saturation Contours

Different gas hydrate regimes can be delineated in two plots (figs. 13 and 15) using appropriately scaled dimensionless groups. These plots, however, do not give any quantitative information about gas hydrate saturation (S_h), the volume fraction of gas hydrate within sediment pore space. The parameter space containing gas hydrate in figures 13 and 15 represent steady state conditions. Thus, each point inside these fields corresponds to a unique depth profile of gas hydrate saturation. Most profiles (for example, figs. 7, 8 and 9) exhibit variable gas hydrate saturation with depth. To get average gas hydrate saturation, we numerically integrate the saturation profile over the depth of the GHSZ:

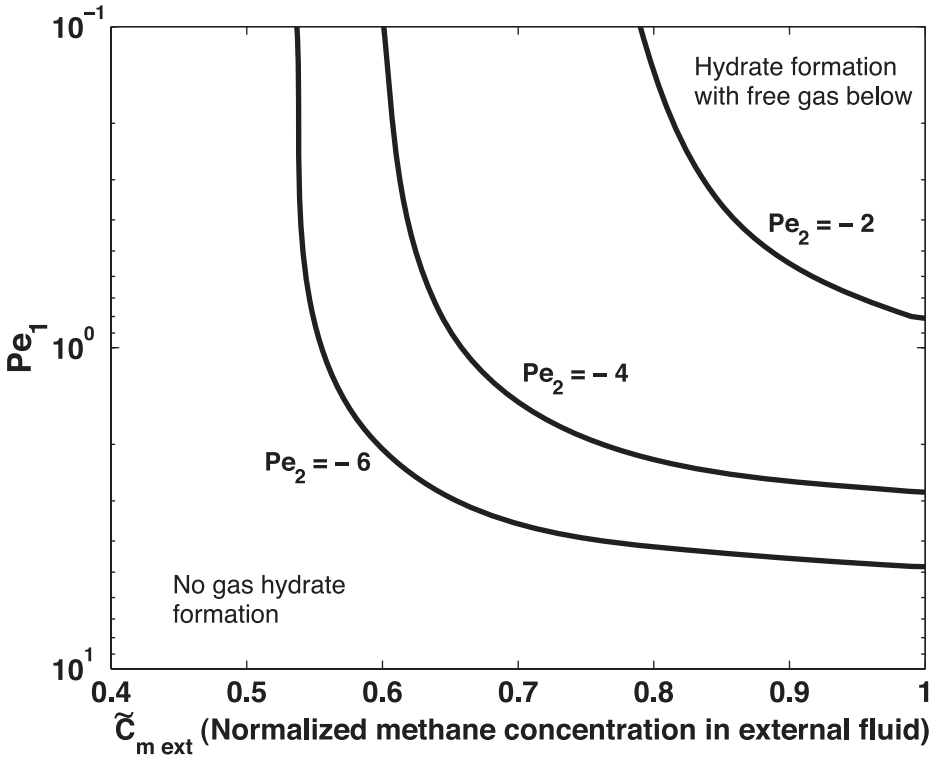

Fig. 14. Parameter space showing curves separating the region of no gas hydrate formation from hydrate formation with free gas below, for methane supplied from deeper sources only ($\beta = 0$, $Da = 0$ and $|Pe_1| < |Pe_2|$). Base case seafloor parameters were used for this simulation.

$$\langle S_h \rangle = \frac{1}{L_t} \int_0^{L_t} S_h(z)\, dz \tag{52}$$

Average gas hydrate saturations were evaluated for several simulations in the gas hydrate forming region of figures 13 and 15. The scaling schemes outlined in previous sections assume even more importance when we observe that average gas hydrate saturation also scales with the dimensionless groups and their combinations, with deviation between saturation contours for different sets of Pe_1/Da of the order of about 5 percent. We plot these saturation contours (for $Pe_1/Da = 0.1$) in figure 16, for methane from *in-situ* sources, along with the set of curves defining the boundaries of the regions in figure 13. The average gas hydrate saturation within the GHSZ increases as Pe_1 or the amount of methane entering the system is increased. It should be emphasized that this single plot of average hydrate saturation suffices for all values of the parameters Pe_1, Da and β.

Average gas hydrate saturations can also be evaluated for cases of external methane supplied from deep sources. The average saturation contours, however, do not scale if we apply the same scaling used to combine different curves in figure 15. This happens because the y-axis in figure 15 represents the total fluid flux into the system, whereas hydrate saturation also depends on the rate at which the sediments are moving. Higher sedimentation rate, characterized by large Pe_1, implies that the gas

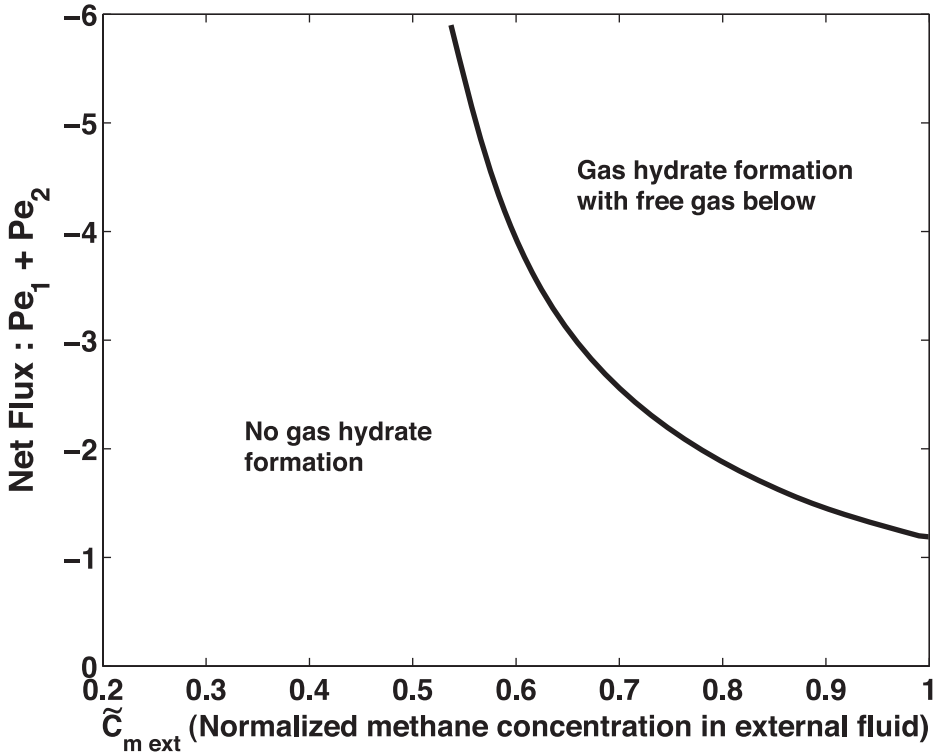

Fig. 15. Single curve separating region of no gas hydrate formation from gas hydrate formation with free gas below by rescaling the y-axis of figure 14, such that it represents the net flux of fluid in the system. The curves corresponding to different Pe_2 in figure 14 come together to yield a single curve for methane supplied from deeper sources ($\beta = 0$, $Da = 0$ and $|Pe_1| < |Pe_2|$). Base case seafloor parameters were used for this simulation.

hydrate layer spends less time in the GHSZ, resulting in lower average hydrate saturation. This causes the average saturation to be strongly dependent on Pe_1, which gets neglected if we take the y-axis to be the sum of Pe_1 and Pe_2. For example, if we simulate a case where $Pe_1 + Pe_2 = -10$, then the average hydrate saturation will be different for the cases [$Pe_1 = 1$, $Pe_2 = -11$], [$Pe_1 = 0.5$, $Pe_2 = -10.5$] and [$Pe_1 = 0.1$, $Pe_2 = -10.1$], although their sum remains the same. The average gas hydrate saturations from the simulations for these cases are 0.4 percent, 0.8 percent and 4 percent, respectively. Although the average gas hydrate saturation is different for each case, we observe that the product of Pe_1 and average saturation remains constant. This means that the quantity that remains invariant is the flux of the gas hydrate, which is simply the product of Pe_1 and the average gas hydrate saturation. Thus, the term $Pe_1 \cdot \langle S_h \rangle$ remains constant and scales with the y-axis of figure 15. The average saturation simulated for several parameters is plotted as contours of constant $Pe_1 \cdot \langle S_h \rangle$ in figure 17. The average saturation can be calculated from these contours by dividing the contour value by Pe_1. It should be noted that we always include the effects of sedimentation when modeling methane from deeper sources. Thus, the results shown in figure 17 hold for the case of finite sedimentation and the problem of singularity when $Pe_1 = 0$ is avoided. We also observe a lower limit to the values of Pe_1 for which the average gas hydrate saturation scales with Pe_1. For very low values of Pe_1, the gas hydrate saturation might approach 100 percent of the pore space, at which point the assumptions of our

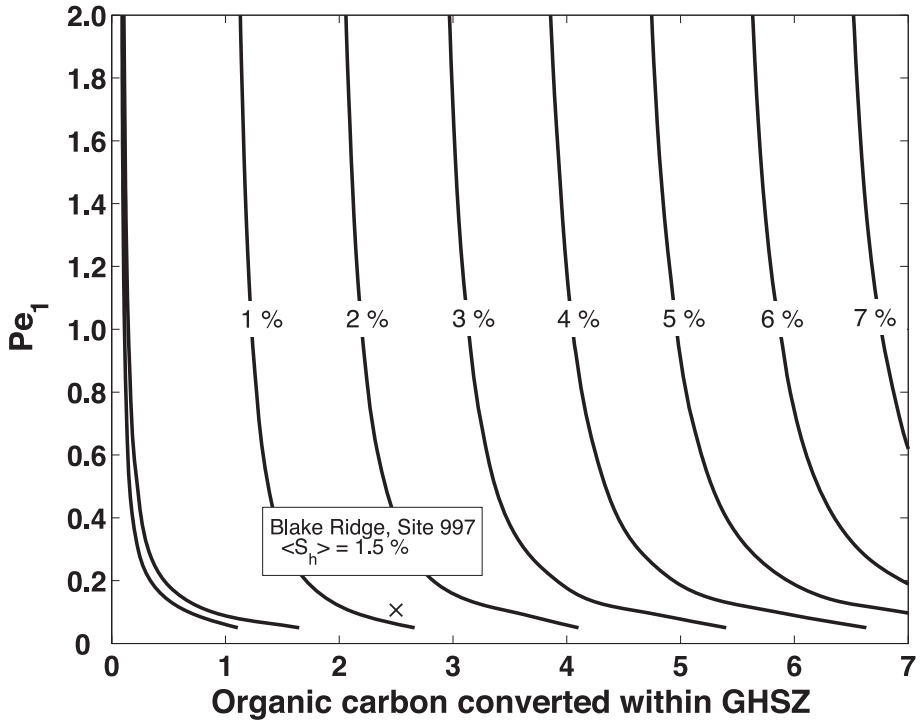

Fig. 16. Average gas hydrate saturation (eq 52) contours plotted for the case of biogenic methane generated *in-situ* ($Pe_2 = 0$). The set of curves plotted in figure 13 are also shown on the left side of the diagram. Base case seafloor parameters were used for this simulation.

model do not hold. The contours shown in figure 17 are valid for $Pe_1 > 0.01$ and $\langle S_h \rangle < 1$. At steady state, average gas hydrate saturation is independent of $\tilde{c}_{m,ext}$ in the external pore fluid. If the external methane concentration is slightly more than the minimum required to precipitate gas hydrate, it takes much longer integration times to achieve the steady state saturation value.

Comparison with Field Data

Average gas hydrate saturations predicted from our simulations can be compared with values inferred from known gas hydrate systems. We consider two well-studied examples: outer Blake Ridge and Cascadia Margin.

Outer Blake Ridge is a sediment drift deposit located offshore on the southeast United States noted for shallow sequences holding abundant methane and gas hydrate (Dickens and others, 1997; Paull and Matsumoto, 2000). Although high fluid advection clearly occurs in some localized areas (for example, ODP Site 996, Paull and others, 1996), the sediment sequence in most places appears characterized by low fluid advection (Egeberg and Dickens, 1999). This inference is supported by the relatively deep but linear pore water sulfate gradients in shallow sediments (Borowski and others, 1996), and the shape of pore water Br and I profiles (Egeberg and Dickens, 1999). The sediments contain a modest amount of organic carbon (TOC between 0.5–1.5%), and gas and pore water chemistry suggests significant biogenic production of methane (Paull and others, 1996). Hence, we model Blake Ridge as an end-member case of a gas hydrate system dominated by *in-situ* methane generation. Previous numerical simulations for gas hydrate accumulation, tailored to ODP Site 997, have

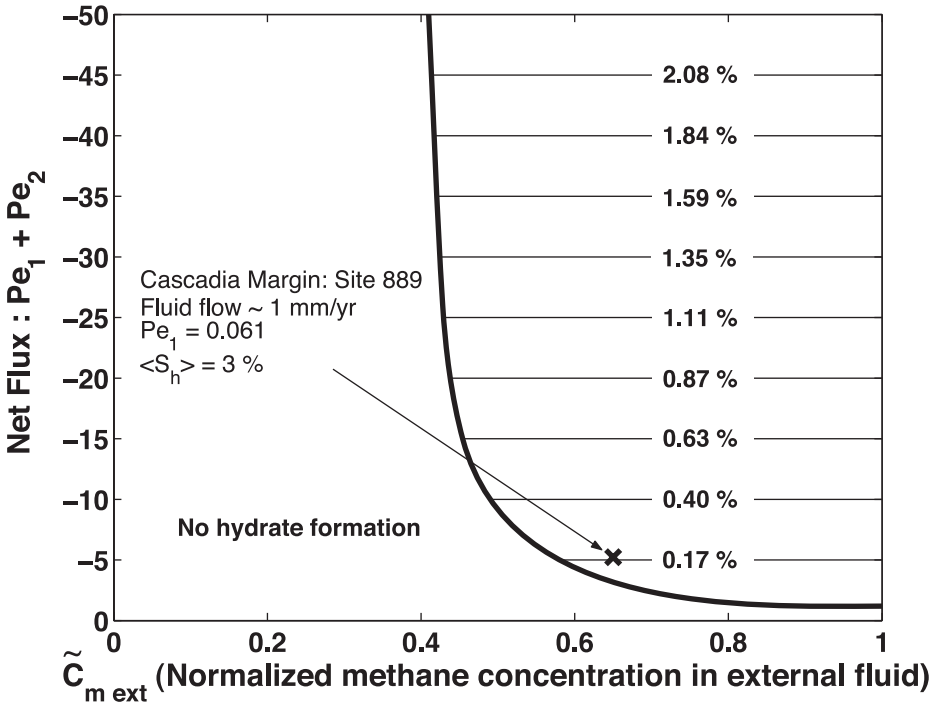

Fig. 17. Contours of gas hydrate flux $Pe_1\langle S_h \rangle$ plotted along with the curves separating the two regions of gas hydrate occurrence in figure 15 for the case of non-zero sedimentation and $|Pe_1| < |Pe_2|$. Gas hydrate saturation can be calculated by dividing the contour values with Pe_1. For example, if $Pe_1 = 1$, these contours directly represent the average gas hydrate saturation in the pore space. Base case seafloor parameters were used for this simulation.

been able to successfully match the abundance of gas hydrate in sediment at this location using an *in-situ* biogenic methane source, sedimentation and diffusion (Egeberg and Dickens, 1999; Davie and Buffett, 2001).

To obtain profiles and average hydrate saturation (fig. 16) for a particular site where *in situ* methanogenesis dominates, the main parameters needed are Pe_1, Da, β, the porosity profile, pore water salinity, seafloor depth, seafloor temperature, and the geotherm. The dimensionless groups, in turn, depend on sedimentation rate, methanogenesis rate, seafloor organic carbon content, depth of GHSZ, methane solubility at the base of GHSZ, and methane diffusivity in pore water. Values of these parameters can be found in the literature for Site 997 (Blake Ridge, table 2). Site 997 was chosen because it is well characterized (Paull and Matsumoto, 2000) and allows comparison with previous simulation results (Davie and Buffett, 2001).

Using site-specific parameters for Site 997, Pe_1 is about 0.1, implying a diffusion dominated system. Following Davie and Buffett (2001), we assume that seafloor TOC is 1.5 weight percent and that 75 percent of this carbon is available for methanogenesis. The amount of organic carbon converted within the GHSZ (eq 51) due to this carbon input is about 2.5 normalized units, which locates Site 997 on the contour plot (fig. 16) at about 1.5 percent average hydrate saturation. Numerical simulation for the above set of parameters was also performed to obtain the hydrate saturation profile (fig. 18), which shows that the peak saturation at the base of GHSZ is close to 5 percent.

It should be noted again that the contour saturations in figure 16 are averaged over the entire GHSZ, and that the peak gas hydrate saturation at the base of the GHSZ

TABLE 2

Model Parameters	Blake Ridge (Site 997)		Cascadia Margin (Site 889)	
	Value	Reference	Value	Reference
Seafloor depth (m)	2781	1	1311	3
Seafloor temperature (^{o}C)	3.4	1	2.7	3
Geothermal gradient (^{o}C/m)	0.04	1	0.054	3
Depth of GHSZ: L_t (m)	458	*	233	*
Methane solubility at base of GHSZ: $c^{l}_{m,eqb}$	2.7×10^{-3}	*	---	
Sedimentation rate: $\dot{S}$ (cm/k.y.)	22	2	25	5
Methane diffusivity: D_m (m^2/s)	10^{-9}	4	10^{-9}	4
Rate of methanogenesis: λ (s^{-1})	10^{-14}	4	---	
Fluid flux due to sedimentation-compaction: $U_{f,sed}$ (m/s)	2.3×10^{-13}		2.64×10^{-13}	
Net fluid flux: $U_f = v_{f,0}\phi_0$ (m/s)	---		-2.2×10^{-11}	6
TOC: α_0 (%)	1.5	1	0	
Dimensionless groups				
$Pe_1 = \frac{U_{f,sed}L_t}{D_m}$	0.1065		0.06	
$Da = \frac{\lambda L_t^2}{D_m}$	2.1		---	
$Pe_1 + Pe_2 - \frac{U_f L_t}{D_m}$	---		- 5.1	
$\beta = \frac{(3/4)\alpha_0}{c^{l}_{m,eqb}}$	4.16		0	
Organic carbon converted within GHSZ: $(1-\tilde{\alpha})\beta$ (eq 51)	2.5		0	
Average hydrate saturation $< S_h >$ (% of pore space)	1.5		3.0	

* Calculated from thermodynamic model

1) Paull and others (1996); 2) Borowski and others (1996); 3) Westbrook and others (1994); 4) Davie and Buffett (2001); 5) Davie and Buffett (2003a); 6) Wang and others (1993)

* Calculated from thermodynamic model

1) Paull and others (1996); 2) Borowski and others (1996); 3) Westbrook and others (1994); 4) Davie and Buffett (2001); 5) Davie and Buffett (2003a); 6) Wang and others (1993)

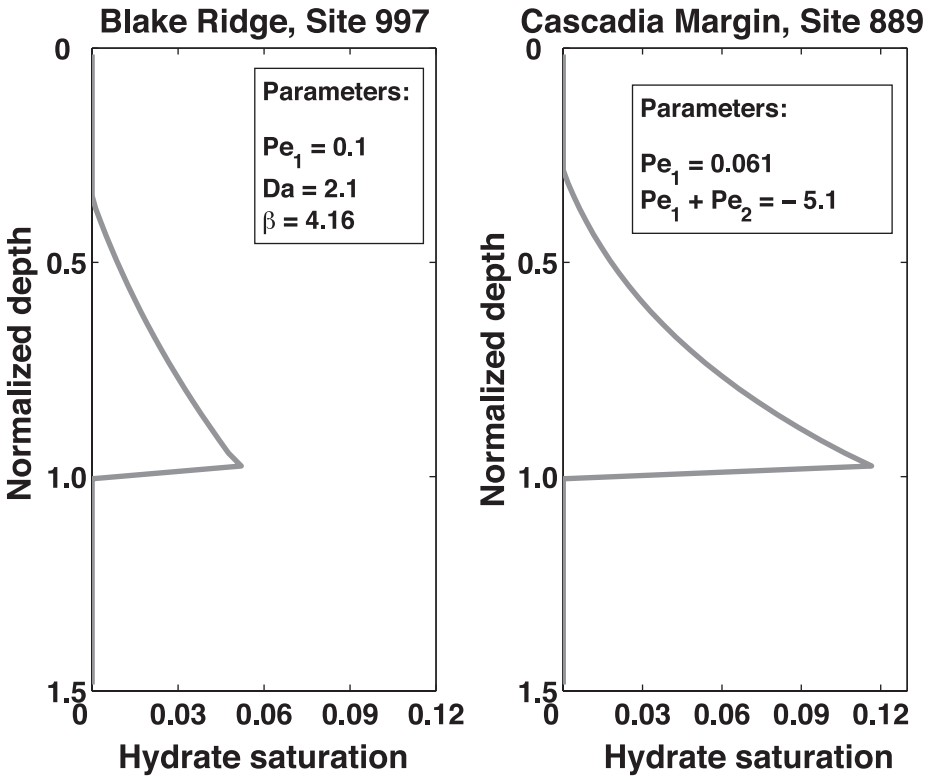

Fig. 18. Steady state hydrate saturation profiles, obtained using the parameters listed in table 2, at Blake Ridge, ODP Site 997 (left) and Cascadia Margin, ODP Site 889 (right)

is usually 3 to 4 times the average value. For an average value of 1.5 percent, this relation implies peak saturation between 4.5 to 6 percent at the base of the GHSZ, which can be verified with the 5 percent peak value from the simulation profile (fig. 18). This value also matches well with the numerical simulations performed by Davie and Buffett (2001). They report average hydrate saturation of about 2 percent for this parameter set, which is in close agreement with the 1.5 percent saturation predicted from our contour map.

The gas hydrate profile and average saturation have been determined for Site 997 using various geophysical/geochemical techniques (Holbrook and others, 1996; Dickens and others, 1997; Egeberg and Dickens, 1999; Collett and Ladd, 2000; Lee, 2000; Paull and others, 2000). Most of these methods yield average gas hydrate saturations of about 2 to 6 percent of the pore space over a gas hydrate occurrence zone between 190 and 450 mbsf (that is, the lower 57% of the entire GHSZ). Our simulation (fig. 18) gives a gas hydrate occurrence zone of 185 to 458 mbsf, and if we average the hydrate saturation profile across this zone, we obtain a value of about 2.4 percent. Hence, our simulation and generalized contour plot (fig. 16) give a good first order estimate of gas hydrate abundance and distribution at Site 997.

The Cascadia Margin is an accretionary margin setting characterized by relatively low TOC content (< 1 %) and relatively high fluid flow rates (Westbrook and others, 1994; Tréhu and others, 2003). Research cruises, including ODP Legs 146 and Leg 204, have not only identified and quantified gas hydrate within sediments of this

region, but have also revealed some surprising aspects concerning gas hydrate distribution. Layers of massive gas hydrate have been found at the southern summit of the Hydrate Ridge where methane actively vents from the seafloor (Tréhu and others, 2003; Haeckel and others, 2004; Torres and others, 2004). These layers are not expected from most numerical models for gas hydrate accumulation, which predict maximum gas hydrate saturations close to the base of the GHSZ (Xu and Ruppel, 1999; Davie and Buffett, 2001). Focused fluid flow through coarse-grained conduits (Tréhu and others, 2004; Milkov and others, 2005) and transport of methane in gas phase through the GHSZ (Haeckel and others, 2004; Torres and others, 2004) has been hypothesized to cause such heterogeneous distributions. The observations and explanations raise interesting issues regarding the presence and migration of free gas within the GHSZ. For example, they may necessitate slow kinetic rates for gas hydrate precipitation and gas dissolution in pore water (Haeckel and others, 2004; Torres and others, 2004) or salinity effects on thermodynamic stability caused by hydrate precipitation (Milkov and others, 2004; Liu and Flemings, 2006). However, apart from specific sites near active seafloor venting, sites in the area appear to be characterized by gas hydrate saturations that increase with depth towards the BSR (Westbrook and others, 1994; Tréhu and others, 2004).

We examine data from ODP Site 889 (Leg 146) west of Vancouver Island (Westbrook and others, 1994) as an example of a gas hydrate system sourced by a deep methane flux. According to our model, the average gas hydrate saturation for this type of source can be constrained with the upward fluid velocity, sedimentation rate, methane diffusivity, the porosity profile, and aforementioned seafloor parameters (table 2). These dimensional variables can be combined into the dimensionless groups, Pe_1 and $Pe_1 + Pe_2$, which are the main parameters controlling the gas hydrate distribution at steady state.

Davie and Buffett (2003a) indicated that an upward velocity of about 0.42 mm/yr ($v_{f,0}$, at the sediment interface) best fits the pore water chlorinity profile at Site 889. This value is similar to that ($\sim$ 1–2 mm/yr) believed to represent the region as a whole (Wang and others, 1993). We use a velocity of 1 mm/yr at the seafloor to get the net fluid flux ($U_f = v_{f,0}\phi_0$, table 2), which characterizes the sum of the two Peclet numbers on the y-axis of the contour plot (fig. 17). The seafloor parameters at this site lead to a predicted GHSZ extending to 233 mbsf, which compares favorably with the BSR depth of 225 mbsf inferred from seismic data (Westbrook and others, 1994). Calculations from the transport parameters give values for $Pe_1 + Pe_2$ and Pe_1 of -5.1 and 0.061, respectively (table 2). This locates the point corresponding to Site 889 at the contour close to $Pe_1\langle S_h\rangle = 0.18\%$ (fig. 17), and implies an average gas hydrate saturation of 3 percent. The gas hydrate profile was also generated (fig. 18), and shows gas hydrate abundance increasing toward 12 percent at the base of GHSZ.

Numerical results from Davie and Buffet (2003a) for parameters close to those listed in table 2 indicate average hydrate saturation between 2 and 5 percent. As explained in their discussion, these modest gas hydrate contents at Site 889 are significantly lower than the 20 to 30 percent saturation above the BSR inferred from certain analyses of seismic velocity and log resistivity (Yuan and others, 1996; Hyndman and others, 1999), but are consistent with the $\sim$ 3 percent value obtained from core temperature measurements (Kastner and others, 1995).

Sensitivity to Seafloor Parameters

All simulations discussed so far have been for constant seafloor depth, bottom water temperature and geothermal gradient. Values of these parameters were taken to be close to those for the crest of Blake Ridge (Paull and others, 1996). We refer to these as the standard or base case values, which are: seafloor depth of 2700 m, seafloor temperature of 3 °C and geothermal gradient of 0.04 °C/m.

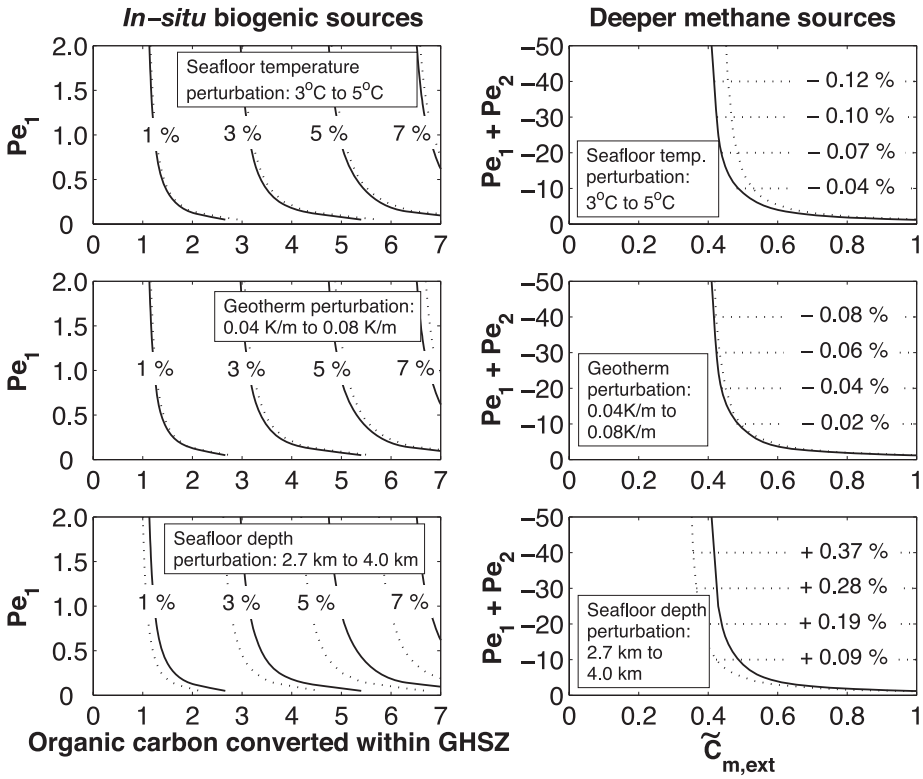

Fig. 19. Sensitivity of the average gas hydrate saturation contours to perturbations in seafloor temperature, geothermal gradient and seafloor depth. The top plot in each column shows the temperature perturbation, the middle represents geotherm perturbation and the bottom represents seafloor depth perturbation. The left column shows contour plots depicting base case saturation contours (solid) and those obtained after applying the perturbation (dotted) for biogenic *in-situ* sources only. The right column shows changes in $Pe_1\langle S_h\rangle$ in response to these perturbations for deeper methane sources. The solid curve represents the boundary between the region of hydrate with free gas and no hydrate for the base case, while the dotted curve is the boundary after applying the perturbation. Change in values of $Pe_1\langle S_h\rangle$ compared to those shown in figure 17 are also listed.

We now show that significant changes in these three parameters cause very small changes to the average hydrate saturation contours shown in figures 16 and 17 for different methane sources. The reason for this behavior is the manner in which we non-dimensionalize the vertical depth in our model using the depth to the GHSZ (L_t) and methane concentration using the peak solubility at the base of the GHSZ. Changes in seafloor parameters can cause a big change in the depth of the GHSZ and peak methane solubility, thus causing a marked change in the methane inputs required to form hydrates. But our scaling scheme transforms these different methane solubility curves into curves that are very similar to each other in the normalized form.

Figure 19 (left column) shows the small change in average saturation contours for biogenic *in-situ* sources caused by large changes in seafloor temperature, geothermal gradient and seafloor depth. The solid curves in each plot represent the base case saturation contours while the dashed curves depict average saturation contours for the perturbed system. It can be seen that average hydrate saturation decreases on increasing seafloor temperature and geothermal gradient, while average hydrate saturation increases on increasing seafloor depth.

Figure 19 (right column) also shows the similar effect of perturbations in seafloor parameters on the saturation contours for methane supplied from deeper sources only. For this case, the three subplots show the boundary separating the region of hydrate with free gas below from the region of no hydrate for the base case (solid) and the perturbed case (dashed). The change in the product $Pe_1 \cdot \langle S_h \rangle$ from the base case is listed on the contours, where positive implies an increase in value of $Pe_1 \cdot \langle S_h \rangle$ after applying the perturbation and negative indicates a decrease in $Pe_1 \cdot \langle S_h \rangle$. Thus, because of the small magnitude of these changes, our simulation results shown in figures 16 and 17 represent very good base cases, with the parameters for any given geological setting acting as small perturbations to the base case.

IMPLICATIONS

By sampling the entire parameter space for each type of methane source, our simulations reveal why natural gas hydrate systems can be so variable. Depending on the methane inputs and outputs, there can be methane-charged sediment sequences containing no gas hydrate, gas hydrate but no free gas below the GHSZ, or gas hydrate with free gas below the GHSZ. The saturations of gas hydrate and free gas are also a function of the dimensionless parameters (figs. 16 and 17).

Some non-intuitive aspects of natural gas hydrate systems can also be understood from our numerical modeling. For example, gas hydrates can precipitate within the GHSZ from *in-situ* sources of methane without a free gas layer below even with continuous sedimentation. Previous modeling had simulated this scenario, but only during the transient part of the simulations (Davie and Buffett, 2001). This happens at steady state conditions, however, when the amount of methane produced is greater than the minimum needed to precipitate gas hydrates but less than the amount required to extend the gas hydrate layer to the base of the GHSZ. This finding has important implications because it suggests that gas hydrate systems can lack a gas hydrate/free gas contact, and hence a BSR on seismic profiles. ODP Site 994 on outer Blake Ridge (Paull and Matsumoto, 2000) may be an example of this situation.

We have also shown that higher sedimentation rates do not necessarily imply higher gas hydrate saturations, at least in the case of *in-situ* methane sources. With the initial TOC context fixed at the seafloor, and the reaction rate fixed with time, increasing sedimentation rates can mean that a higher fraction of organic carbon passes through the GHSZ. This could yield lower gas hydrate saturation at steady state.

Sedimentation rates and TOC input are not constant over geologic time scales. The saturation contour plots (figs. 16 and 17) provide a convenient way to quantitatively examine variations in average gas hydrate saturation resulting from such changes. For example, if the sedimentation rate and TOC input over time are known, one can plot points corresponding to different values of these parameters to see how a particular gas hydrate system would evolve. This procedure, of course, assumes that the gas hydrate system achieved steady state after each change in sedimentation rate and/or TOC input.

OUTSTANDING PROBLEMS

We have incorporated most of the factors believed responsible for gas hydrate accumulation in marine sediments, but some secondary effects remain:

- The formation and dissociation of gas hydrates impacts the salinity of surrounding water, which changes the gas hydrate equilibrium and methane solubility curves (Egeberg and Dickens, 1999; Liu and Flemings, 2006). Dissolved ions and their variation with depth should be coupled into the numerical models. As an extreme example, rapid formation of gas hydrate may generate high pore water salinity, which can allow free gas layers within the GHSZ (Milkov and others, 2004).

- Significant methanogenesis does not begin at the seafloor, but below a SRZ (Borowski and others, 1999). Davie and Buffett (2003b) included a SRZ in their steady state model for gas hydrate accumulation by assuming a constant depth to the sulfate methane interface. However, this assumption is not strictly valid because at initial time, when there is no methane present in the pore waters, the zero sulfate boundary lies deeper in the sediments. As methane accumulates in the pore waters, this depth shifts up due to methane oxidation and responds dynamically to changes in the methane flux (Borowski and others, 1996). Including a SRZ probably has a negligible effect on gas hydrate saturation, but it may help constrain site-specific parameters.
- Clearly, gas hydrate has a heterogeneous distribution in marine sediment at a local scale. These variations probably relate to lateral fluid flow and gas migration in response to differences in permeability. To study these effects, gas hydrate models ultimately will need to be extended to at least two spatial dimensions.

CONCLUSIONS

We have developed a numerical model for predicting gas hydrate formation and accumulation over geologic time scales from methane generated either from biogenic *in-situ* sources, methane from upward external fluxes or both. The following conclusions can be drawn from our simulation results:

- At steady state conditions, marine sequences where all methane comes from *in-situ* microbial activity can be divided into three categories: no gas hydrate, gas hydrate without free gas below and gas hydrate with an underlying free gas layer. The first Peclet number (Pe_1), the Damkohler number (Da) and the organic input at the seafloor control the category.
- For systems where methane derives from an external deep source, the category of gas hydrate without free gas below is not observed at steady state conditions when sedimentation occurs. Decreasing Pe_1 to low values delays the time it takes to achieve steady state, but the steady-state system either has no gas hydrate or gas hydrate directly underlain by a free gas layer at the base of the GHSZ.
- Disconnected gas hydrate and free gas layers are observed in our external flux simulations if we set sedimentation to zero ($Pe_1 = 0$), because this causes the gas hydrate and free gas layers to become immobile. Consistent with the results of Xu and Ruppel (1999), a critical external flux has to be exceeded to extend the gas hydrate and free gas layers to the base of the GHSZ.
- Gas hydrate distribution depends on various parameters but can be summarized in two plots, one each for *in-situ* and deeper methane sources, by appropriately combining dimensionless groups. For biogenic *in-situ* sources, this happens when Pe_1 is plotted against the amount of organic carbon converted within the GHSZ (eq 51). For deeper methane sources, this happens when the net flux ($Pe_1 + Pe_2$) is plotted against the methane concentration of the external flux.
- Average gas hydrate saturation contours also scale with dimensionless groups, so that two contour maps provide gas hydrate saturation values for a large range of parameters. These contour maps are relatively insensitive to changes in seafloor temperature, depth and geothermal gradients, and are thus applicable to a wide variety of geological settings. Site-specific simulations done by other investigators (Davie and Buffett, 2001, 2003a) become single points on these saturation maps. Our scaling schemes make these plots ideal base cases for providing quantitative information about the possible types of hydrate accumulation at any given location without performing any numerical simulations. This turns out to be a big improvement over most of the site-specific results available from hydrate modeling in the literature, which are valid only for the numerous parameters relevant to a particular gas hydrate province.

ACKNOWLEDGMENTS

We gratefully acknowledge the Shell Center for Sustainability, the Kobayashi Graduate Fellowship, and the Department of Energy for financially supporting this work. We also thank Bernard Boudreau, Matthias Haeckel and an anonymous reviewer for constructive and critical reviews that significantly improved this manuscript.

References

Adisasmito, S., Frank, R. J., and Sloan, Jr., E. D., 1991, Hydrates of carbon dioxide and methane mixtures: Journal of Chemical and Engineering Data, v. 36, p. 68–71.

Audet, D. M., and Fowler, A. C., 1992, A mathematical model for compaction in sedimentary basins: Geophysical Journal International, v. 110, p. 577–590.

Berner, R. A., 1980, Early diagenesis: A theoretical approach: Princeton, New Jersey, Princeton University Press, 241 p.

Bethke, C. M., 1985, A numerical model of compaction-driven groundwater flow and heat transfer and its application to the Paleohydrology of intracratonic sedimentary basins: Journal of Geophysical Research, v. 90, p. 6817–6828.

Borowski, W. S., and Paull, C. K., 1997, The gas hydrate detection problem: Recognition of shallow-subbottom gas hazards in deep-water areas: Proceedings of the Offshore Technology Conference, v. 1 OTC-8297, p. 211–216.

Borowski, W. S., Paull, C. K., and Ussler, W. III, 1996, Marine pore-water sulfate profiles indicate *in situ* methane flux from underlying gas hydrate: Geology, v. 24, p. 655–658.

——— 1999, Global and local variations of interstitial sulfate gradients in deep-water, continental margin sediments: Sensitivity to underlying methane and gas hydrates: Marine Geology, v. 159, p. 131–154.

Boudreau, B. P., 1997, Diagenetic models and their implementation: Berlin, Springer-Verlag, 414 p.

Boudreau, B. P., and Bennett, R. H., 1999, New rheological and porosity equations for steady-state compaction: American Journal of Science, v. 299, p. 517–528.

Briaud, J. L., and Chaouch, A., 1997, Hydrate melting in soil around hot conductor: Journal of Geotechnical and Geoenvironmental Engineering, v. 123, p. 645–653.

Buffett, B. A., and Archer, D., 2004, Global inventory of methane clathrate: Sensitivity to changes in the deep ocean: Earth and Planetary Science Letters, v. 227, p. 185–199.

Cao, Z., Tester, J. W., and Trout, B. L., 2002, Sensitivity analysis of hydrate thermodynamic reference properties using experimental data and *ab initio* methods: Journal of Physical Chemistry B, v. 106, p. 7681–7687.

Claypool, G. E., and Kvenvolden, K. A., 1983, Methane and other hydrocarbon gases in marine sediment: Annual Review of Earth and Planetary Sciences, v. 11, p. 299–327.

Clennell, M. B., Hovland, M., Booth, J. S., Henry, P., and Winters, W. J., 1999, Formation of natural gas hydrates in marine sediments 1. Conceptual model of gas hydrate growth conditioned by host sediment properties: Journal of Geophysical Research, v. 104, p. 22985–23003.

Collett, T. S., 2002, Energy resource potential of natural gas hydrates: AAPG Bulletin, v. 86, p. 1971–1992.

Collett, T. S., and Ladd, J., 2000, Detection of gas hydrate with downhole logs and assessment of gas hydrate concentrations (saturations) and gas volumes on the Blake Ridge with electrical resistivity log data, *in* Paull, C. K., Matsumoto, R., Wallace, P. J., and Dillon, W. P., editors: Proceedings of the Ocean Drilling Program, Scientific Results, v. 164, p. 179–191.

Davie, M. K., and Buffett, B. A., 2001, A numerical model for the formation of gas hydrate below the seafloor: Journal of Geophysical Research, v. 106, p. 497–514.

——— 2003a, Sources of methane for marine gas hydrate: inferences from a comparison of observations and numerical models: Earth and Planetary Science Letters, v. 206, p. 51–63.

——— 2003b, A steady state model for marine hydrate formation: Constraints on methane supply from pore water sulfate profiles: Journal of Geophysical Research, v. 108(B10), 2495, doi:10.1029/2002JB002300.

Davie, M. K., Zatsepina, O. Y., and Buffett, B. A., 2004, Methane solubility in marine hydrate environments: Marine Geology, v. 203, p. 177–184.

de Roo, J. L., Peters, C. J., Lichtenthaler, R. N., and Diepen, G. A. M., 1983, Occurrence of methane hydrate in saturated and unsaturated solutions of sodium chloride and water in dependence of temperature and pressure: AICHE Journal, v. 29(4), p. 651–657.

Dickens, G. R., 2001, The potential volume of oceanic methane hydrates with variable external conditions: Organic Geochemistry, v. 32, p. 1179–1193.

——— 2003, Rethinking the global carbon cycle with a large, dynamic and microbially mediated gas hydrate capacitor: Earth and Planetary Science Letters, v. 213, p. 169–183.

Dickens, G. R., and Quinby-Hunt, M. S., 1994, Methane hydrate stability in seawater: Geophysical Research Letters, v. 21, p. 2115–2118.

Dickens, G. R., O'Neil, J. R., Rea, D. K., and Owen, R. M., 1995, Dissociation of oceanic methane hydrate as a cause of the carbon isotope excursion at the end of the Paleocene: Paleoceanography, v. 10, p. 965–971.

Dickens, G. R., Paull, C. K., Wallace, P., and the ODP Leg 164 Scientific Party, 1997, Direct measurement of *in situ* methane quantities in a large gas-hydrate reservoir: Nature, v. 385, p. 426–428.

Duan, Z., Moller, N., Greenberg, J., and Weare, J. H., 1992, The prediction of methane solubility in natural waters to high ionic strength from 0 to 250°C and from 0 to 1600 bar: Geochimica et Cosmochimica Acta, v. 56, p. 1451–1460.

Egeberg, P. K., and Dickens, G. R., 1999, Thermodynamic and pore water halogen constraints on hydrate distribution at ODP Site 997 (Blake Ridge): Chemical Geology, v. 153, p. 53–79.
Flemings, P. B., Liu, X., and Winters, W. J., 2003, Critical pressure and multiphase flow in Blake Ridge gas hydrates: Geology, v. 32(12), p. 1057–1060.
Gering, K. L., 2003, Simulations of methane hydrate phenomena over geologic timescales. Part I: Effect of sediment compaction rates on methane hydrate and free gas accumulations: Earth and Planetary Science Letters, v. 206, p. 65–81.
Gibson, R. E., 1958, The progress of consolidation in a clay layer increasing in thickness with time: Geotechnique, v. 8, p. 171–182.
Haeckel, M., Suess, E., Wallman, K., and Rickert, D., 2004, Rising methane gas bubbles form massive hydrate layers at the seafloor: Geochimica et Cosmochimica Acta, v. 68, p. 4335–4345.
Handa, Y. P., 1990, Effect of hydrostatic pressure and salinity on the stability of gas hydrates: Journal of Physical Chemistry, v. 94, p. 2652–2657.
Hesselbo, S. P., Gröcke, D. R., Jenkyns, H. C., Bjerrum, C. J., Farrimond, P., Morgans Bell, H. S., and Green, O. R., 2000, Massive dissociation of gas hydrates during a Jurassic oceanic anoxic event: Nature, v. 406, p. 392–395.
Holbrook, W. S., Hoskins, H., Wood, W. T., Stephen, R. A., Lizzaralde, D., and Leg 164 Science Party, 1996, Methane hydrate and free gas on the Blake Ridge from vertical seismic profiling: Science, v. 273, p. 1840–1843.
Holder, G. D., Corbin, G., and Papadopoulos, K. D., 1980, Thermodynamic and molecular properties of gas hydrates from mixtures containing methane, argon and krypton: Industrial and Engineering Chemistry Fundamentals, v. 19, p. 282–286.
Hutchison, I., 1985, The effect of sedimentation and compaction on oceanic heat flow: Geophysical Journal of the Royal Astronomical Society, v. 82, p. 439–459.
Hyndman, R. D., and Davis, E. E., 1992, A mechanism for the formation of methane hydrate and seafloor bottom-simulating reflectors by vertical fluid expulsion: Journal of Geophysical Research B, v. 97, p. 7025–7041.
Hyndman, R. D., Yuan, T., and Moran, K., 1999, The concentration of deep sea gas hydrates from downhole electrical resistivity logs and laboratory data: Earth and Planetary Science Letters, v. 172, p. 167–177.
Kastner, M., Kvenvolden, K. A., Whiticar, M. J., Camerlenghi, A., and Lorenson, T. D., 1995, Relation between pore fluid chemistry and gas hydrates associated with bottom-simulating reflectors at the Cascadia Margin, Sites 889 and 892, *in* Carson, B., Westbrook, G. K., Musgrave, R. J., and Suess, E., editors: Proceedings of the Ocean Drilling Program, Scientific Results, v. 146 (pt. 1), p. 175–187.
Klauda, J. B., and Sandler, S. I., 2005, Global distribution of methane hydrate in ocean sediment: Energy and Fuels, v. 19, p. 459–470.
Kraemer, L. M., Owen, R. M., and Dickens, G. R., 2000, Lithology of the upper gas hydrate zone, Blake Outer Ridge: A link between diatoms, porosity, and gas hydrate: Proceedings of the Ocean Drilling Program Scientific Results, v. 164, p. 229–236.
Kvenvolden, K. A., 1988, Methane hydrate – A major reservoir of carbon in the shallow geosphere?: Chemical Geology, v. 71, p. 41–51.
——— 1993, Gas hydrates: Geological perspective and global change: Reviews of Geophysics, v. 31, p. 173–187.
Lee, M. W., 2000, Gas hydrates amount estimated form acoustic logs at the Blake Ridge, Sites 994, 995, and 997, *in* Paull, C. K., Matsumoto, R., Wallace, P. J., and Dillon, W. P., editors: Proceedings of the Ocean Drilling Program, Scientific Results, v. 164, p. 193–198.
Liu, X., and Flemings, P. B., 2006, Passing gas through the hydrate stability zone at southern Hydrate Ridge, offshore Oregon: Earth and Planetary Science Letters, v. 241, p. 211–226.
Luff, R., and Wallmann, K., 2003, Fluid flow, methane fluxes, carbonate precipitation and biogeochemical turnover in gas hydrate-bearing sediments at Hydrate Ridge, Cascadia Margin: Numerical modeling and mass balances: Geochimica et Cosmochimica Acta, v. 67, p. 3403–3421.
Marshall, D. R., Saito, S., and Kobayashi, R., 1964, Hydrates at high pressure, part i: Methane-water, argon-water, and nitrogen-water system: AICHE Journal, v. 10, p. 202–205.
Martens, C. S., and Berner, R. A., 1977, Interstitial water chemistry of anoxic Long Island Sound sediments. 1. Dissolved gases: Limnology and Oceanography, v. 22, p. 10–25.
Maslin, M., Owen, M., Day, S., and Long, D., 2004, Linking continental-slope failures and climate change: Testing the clathrate gun hypothesis: Geology, v. 32, p. 53–56.
McLeod, H. O., and Campbell, J. M., 1961, Natural gas hydrates at pressures to 10,000 psia: Journal of Petroleum Technology, v. 13, p. 590–595.
Milkov, A. V., 2004, Global estimates of hydrate-bound gas in marine sediments: how much is really out there?: Earth-Science Reviews, v. 66, p. 183–197.
——— 2005, Molecular and stable isotope compositions of natural gas hydrates: A revised global dataset and basic interpretations in the context of geological settings: Organic Geochemistry, v. 36, p. 681–702.
Milkov, A. V., and Sassen, R., 2000, Thickness of the gas hydrate stability zone, Gulf of Mexico continental slope: Marine Geology, v. 17, p. 981–991.
Milkov, A. V., Claypool, G. E., Lee, Y. J., Xu, W., Dickens, G. R., Borowski, W. S., and ODP Leg 204 Scientific Party, 2003, *In situ* methane concentrations at Hydrate Ridge, offshore Oregon: New constraints on the global gas hydrate inventory from an active margin: Geology, v. 31(10), p. 833–836.
Milkov, A. V., Dickens, G. R., Claypool, G. E., Lee, Y. J., Borowski, W. S., Torres, M. E., Xu, W., Tomaru, H., Tréhu, A. M., and Schultheiss, P., 2004, Co-existence of gas hydrate, free gas, and brine within the regional gas hydrate stability zone at Hydrate Ridge (Oregon Margin): evidence from prolonged degassing of a pressurized core: Earth and Planetary Science Letters, v. 222, p. 829–843.

Milkov, A. V., Claypool. G. E., Lee, Y. J., and Sassen, R., 2005, Gas hydrate systems at Hydrate Ridge offshore Oregon inferred from molecular and isotopic properties of hydrate-bound and void gases: Geochimica et Cosmochimica Acta, v. 69, p. 1007–1026.

Parrish, W. R., and Prausnitz, J. M., 1972, Dissociation pressures of gas hydrates formed by gas mixtures: Industrial and Engineering Chemistry Process Design and Development, v. 11(1), p. 26–35.

Paull, C. K., and Matsumoto, R., 2000, Leg 164 Overview: Proceedings of the Ocean Drilling Program, Scientific Results, v. 164, p. 3–10.

Paull, C. K., Ussler, W., III, and Borowski, W. S., 1994, Source of methane to form marine gas hydrates, *in* Sloan, E. D., Happel Jr., J., and Hnatow, M. A., editors, Natural Gas Hydrates: Annals of the New York Academy of Sciences, v. 715, p. 392–409.

Paull, C. K., Matsumoto, R., Wallace, P. J., and Dillon, W. P., 1996: College Station, Texas, Proceedings of the Ocean Drilling Program, Initial Reports, v. 164.

Peng, D. Y., and Robinson, D. B., 1976, A new two-constant equation of state: Industrial and Engineering Chemistry Fundamentals, v. 1(15), p. 59–64.

Pitzer, K. S., and Mayorga, G., 1973, Thermodynamics of electrolytes. II. Activity and osmotic coefficients for strong electrolytes with one or both ions univalent: Journal of Physical Chemistry, v. 77(19), p. 2300–2308.

Rempel, A. W., and Buffett, B. A., 1997, Formation and accumulation of gas hydrate in porous media: Journal of Geophysical Research, v. 102, p. 10151–10164.

Rubey, W. W., and Hubbert, M. K., 1959, Role of fluid pressure in mechanics of over-thrust faulting; ii. Overthrust belt in geosynclinal area of western Wyoming in light of fluid pressure hypothesiss: Geological Society of America Bulletin, v. 70, p. 167–206.

Seo, Y., Lee, H., and Ryu, B. J., 2002, Hydration number and two-phase equilibria of CH_4 hydrate in the deep ocean sediments: Geophysical Research Letters, v. 29(8), p. 1244.

Servio, P., and Englezos, P., 2002, Measurement of dissolved methane in water in equilibrium with its hydrate: Journal of Chemical and Engineering Data, v. 47, p. 87–90.

Sloan, E. D., 1998, Clathrate hydrates of natural gases: New York, Marcel Dekker, 726 p.

Sultan, N., Cochonat, P., Foucher, J. P., and Mienert, J., 2004, Effect of gas hydrates melting on seafloor slope instability: Marine Geology, v. 213, p. 379–401.

Terzaghi, K., 1943, Theoretical Soil Mechanics: New York, Wiley, 528 p.

Tishchenko, P., Hensen, C., Wallmann, K., and Wong, C. S., 2005, Calculation of the stability and solubility of methane hydrate in seawater: Chemical Geology, v. 219, p. 37–52.

Torres, M. E., Wallman, K., Tréhu, A. M., Bohrmann, G., Borowski, W. S., and Tomaru, H., 2004, Gas hydrate growth, methane transport, and chloride enrichment at the southern summit of Hydrate Ridge, Cascadia margin off Oregon: Earth and Planetary Science Letters, v. 226, p. 225–241.

Tréhu, A. M., Bohrmann, G., Rack, F., and Torres, M. E., 2003: Proceedings of the Ocean Drilling Program, Initial Reports, v. 204.

Tréhu, A. M., Long, P. E., Torres, M. E., Bohrmann, G., Rack, F. R., Collett, T. S., Goldberg, D. S., Milkov, A. V., Riedel, M., Schultheiss, P., Bangs, N. L., Barr, S. R., Borowski, W. S., Claypool, G. E., Delwiche, M. E., Dickens, G. R., Gracia, E., Guerin, G., Holland, M., Johnson, J. E., Lee, Y. J., Liu, C. S., Su, X., Teichert, B., Tomaru, H., Vanneste, M., Watanabe, M., and Weinberger, J. L., 2004, Three-dimensional distribution of gas hydrate beneath southern Hydrate Ridge: constraints from ODP Leg 204: Earth and Planetary Science Letters, v. 222, p. 845–862.

van der Waals, J. H., and Platteeuw, J. C., 1959, Clathrate solutions: Advances in Chemical Physics, v. 2, p. 1–57.

Wallmann, K., Aloisi, G., Haeckel, M., Obzhirov, A., Pavlova, G., and Tishchenko, P., 2006, Kinetics of organic matter degradation, microbial methane generation, and gas hydrate formation in anoxic marine sediments: Geochimica et Cosmochimica Acta, v. 70, p. 3905–3927.

Wang, K., Hyndman, R. D., and Davis, E. E., 1993, Thermal effects of sediment thickening and fluid expulsion in accretionary prisms: model and parameter analysis: Journal of Geophysical Research, v. 98, p. 9975–9984.

Wangen, M., 1992, Pressure and temperature evolution in sedimentary basins: Geophysical Journal International, v. 110, p. 601–613.

Weinberger, J. L., Brown, K. M., and Long, P. E., 2005, Painting a picture of gas hydrate distribution with thermal images: Geophysical Research Letters, v. 32, L04609, doi:10.1029/2004GL021437.

Westbrook, G. K., Carson, B., Musgrave, R. J., and others, 1994: Proceedings of the Ocean Drilling Program, Initial Reports, v. 146 (Pt. 1).

Whiticar, M. J., Faber, E., and Schoell, M., 1986, Biogenic methane formation in marine and freshwater environments: CO_2 reduction vs. acetate fermentation - Isotope evidence: Geochimica et Cosmochimica Acta, v. 50, p. 693–709.

Xu, W., and Ruppel, C., 1999, Predicting the occurrence, distribution, and evolution of methane gas hydrate in porous marine sediments: Journal of Geophysical Research, v. 104, p. 5081–5096.

Yang, S. O., Cho, S. H., Lee, H., and Lee, C. S., 2001, Measurement and prediction of phase equilibria for water + methane in hydrate forming conditions: Fluid Phase Equilibria, v. 185, p. 53–63.

Yuan, T., Hyndman, R. D., Spence, G. D., and Desmons, B., 1996, Seismic velocity increase and deep-sea gas hydrate concentration above a bottom-simulating reflector on the northern Cascadia continental slope: Journal of Geophysical Research, v. 101, p. 13655–13671.

Zatsepina, O. Y., and Buffett, B. A., 1998, Thermodynamic conditions for the stability of gas hydrate in the seafloor: Journal of Geophysical Research, v. 103, p. 24127–24139.